

**IMPROVEMENT OF TRANSPARENT
CONDUCTIVE HYBRID ITO/Ag/ITO
ELECTRODES BY ELECTRO-ANNEALING**

**A Thesis Submitted to
the Graduate School of Engineering and Sciences of
İzmir Institute of Technology
in Partial Fulfillment of the Requirements for the Degree of**

MASTER OF SCIENCE

in Physics

**by
Zemzem UYANIK**

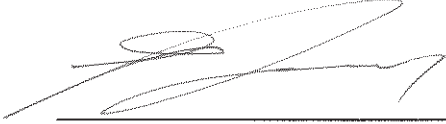
**July 2019
İZMİR**

We approve the thesis of **Zemzem UYANIK**

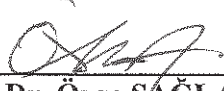
Examining Committee Members:



Prof. Dr. Gülnur AYGÜN ÖZYÜZER
Department of Physics, İzmir Institute of Technology

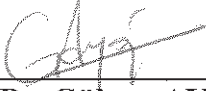


Asst. Prof. Dr. Enver TARHAN
Department of Physics, İzmir Institute of Technology

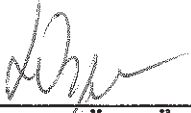


Asst. Prof. Dr. Özge SAĞLAM
Department of Mechanical Engineering, İzmir University of Economics

01 July 2019



Prof. Dr. Gülnur AYGÜN ÖZYÜZER
Supervisor, Department of Physics
Izmir Institute of Technology



Prof. Dr. Lütfi ÖZYÜZER
Head of the Department of Physics

Prof. Dr. Aysun SOFUOĞLU
Dean of the Graduate School of
Engineering and Science

ACKNOWLEDGMENTS

I would like to express my gratitude to Prof. Dr. Gülnur AYGÜN ÖZYÜZER for her guidance over the past two years and my special thank to Prof. Dr. Lütfi ÖZYÜZER for the enlightening discussions, constant encouragement and the valuable tutorial he has given me. The personal library of his was a constant source of useful books.

I wish to thank my thesis committee members: Asst. Prof. Dr. Enver TARHAN and Asst. Prof. Dr. Özge SAĞLAM for their valuable feedback and advice.

I would like to thank Hasan KÖSEOĞLU for his advice in my thesis procedure.

I appreciate to the specialists at IZTECH-Center of Materials Research for the SEM and XRD analysis.

My deepest thanks to my close friend Yeşim ALDURAN who was always near to me in my career challenges.

I am grateful to Prof. Dr. ÖZYÜZER's group at the University of IZTECH for their valuable collaboration and technical support. Especially, I am greatly indebted to my colleagues Bengü ATA. Special thanks to my group members, J. Enrique Mtz. MEDINA, Aileen NOORİ, Ece MERİÇ, Çağlar GEDİKSİZ.

Many thanks and love to my mother, my father, my sister and my brother for their permanent support, understanding, always trusting, and encouraging me in every moment of my life and dedicated my thesis to my family and childhood friend.

My sincere appreciation to my beloved friend Fatih TÜRKMEN for believing in me and for his love and fully supports. Keep on smile.

This study was partially supported by The Scientific and Technological Research Council of Turkey (TUBITAK) with the project number of 215E113 and Teknoma Technological Materials Inc.

ABSTRACT

IMPROVEMENT OF TRANSPARENT CONDUCTIVE HYBRID ITO/Ag/ITO ELECTRODES BY ELECTRO-ANNEALING

The optical and electrical performances of hybrid ITO/Ag/ITO (IAI) layer structures have been investigated as a function of the Ag and ITO film thicknesses. The IAI films have been prepared by dc magnetron sputtering at room temperature on borosilicate glass under high vacuum. The thickness of ITO, Ag, ITO films in the hybrid structure were adjusted to have low sheet resistance and high optical transmittance. The deposited metal Ag layer between two ITO layers with thicknesses ranging from 10 to 25 nm has been used. After analyzing IAI multilayer, electro-annealing was applied to improve the crystallinity of the obtained IAI films and it was aimed to increase the lifetime of the electronic device by investigating the effect of electrical current on IAI films and it has shown that electro-annealing is a more suitable technique for industrial applications. Optoelectronic performance result of high quality electrode shows that the sheet resistance of IAI films was improved down to $8.7 \Omega/\square$ after the electro-annealing. Furthermore, the highest transmittance of 88.9% was achieved and the optical properties of the hybrid IAI thin films depend on Ag thicknesses that alter the ITO film crystallinity.

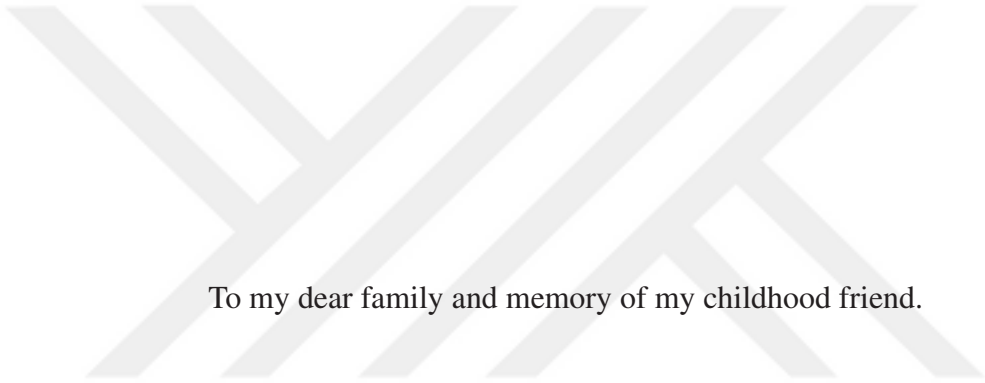
The structural properties of IAI films have been characterized as a function of annealing temperature by X-ray diffraction (XRD). Information about the morphology of IAI thin film was carried by scanning electron microscope (SEM). Optical properties were measured with spectrophotometer having the wavelength range of 200-2600 nm. For surface resistance measurements, the four point method was applied using Keithley 2424 sourcemeter.

ÖZET

GEÇİRGEN İLETKEN HİBRİT ITO/Ag/ITO ELEKTROTLARIN ELEKTRO-TAVLAMA İLE İYİLEŞTİRİLMESİ

Hibrit ITO/Ag/ITO (IAI) ince film tabaka yapılarının optik ve elektriksel performansları, ITO ve Ag katman kalınlığının fonksiyonu olarak incelenmiştir. Hibrit IAI ince filmleri borosilikat cam üzerine oda sıcaklığında yüksek vakum altında dc manyatısal saçtırma yöntemi ile üretilmiştir. Hibrit yapıdaki ITO, Ag, ITO filmlerin kalınlığı düşük tabaka direncine ve yüksek optik geçirgenliğe sahip olacak şekilde ayarlanmıştır. ITO katmanları arasındaki gömülü metal Ag katmanı, 10 nm ile 25 nm arasında değişen kalınlıklarda kullanılmıştır. IAI tabakası analiz edildikten sonra IAI ince filmlerin kristallliğini iyileştirmek için elektro-tavlama uygulanmıştır ve elektrik akımının IAI ince filmler üzerindeki etkisinin araştırılmasıyla elektronik cihaz ömrünün artırılması amaçlanmıştır. Elektro-tavlamanın endüstriyel uygulamalar için daha uygun bir teknik olduğu sonucuna varılmıştır. IAI ince filmin yüzey direnci elektro-tavlama işleminden sonra $8.7 \Omega/\square$ olarak bulunmuştur en yüksek geçirgenliğe ise %88.9'ya ulaşılmıştır. Hibrit IAI ince filmlerin optoelektronik özellikleri, ITO film kristallliğini etkileyen ara katman olan metal Ag kalınlığına bağlıdır.

Hibrit IAI ince filmlerinin yapısal özellikleri, $\text{CuK}\alpha$ radyasyonuna sahip ($\lambda=0.154 \text{ nm}$) X-ışını kırınımı (XRD) (Philips X'Pert Pro) ile tavlama sıcaklığının fonksiyonu olarak karakterize edilmiştir. IAI ince filmlerinin morfolojisi hakkında bilgi taramalı elektron mikroskobu (SEM) ile elde edilmiştir. IAI ince filmin optik geçirgenliği 200-2600 nm dalga boyu aralığına sahip PerkinElmerLambda 950 UV/Vis/NIR Spektrofotometre ile ölçülmüştür. Yüzey direnci ölçümleri için Keithley 2424 kaynak metrisi kullanılarak dört nokta yöntemi uygulanmıştır.



To my dear family and memory of my childhood friend.

TABLE OF CONTENTS

LIST OF FIGURES	ix
LIST OF TABLES	xii
CHAPTER 1. INTRODUCTION	1
1.1. Transparent Conductive Oxides	1
1.1.1. Indium Tin Oxide (ITO) Films	3
1.1.2. Aluminum Doped ZnO Thin Films.....	4
1.1.3. Fluorine Doped Tin Oxide (FTO) Thin Films	5
1.1.4. Gallium Doped ZnO Thin Films (GaZO)	6
1.1.5. Graphene as a Transparent Conductor	6
1.1.6. Zinc Tin Oxide (ZTO) Thin Films.....	7
1.2. Transparent Film Heaters (TFHs)	8
1.3. Electro-Annealing	9
1.4. Motivation	10
CHAPTER 2. THEORETICAL BACKGROUND	11
2.1. Indium Oxide and Tin-Doped Indium Oxide	11
2.1.1. Crystal Structure of ITO	11
2.1.2. Body-Centered Cubic Type Structure of ITO	11
2.2. Significant Electronic Levels	13
2.3. Literature Review: Hybrid ITO/Ag/ITO Layer	14
CHAPTER 3. EXPERIMENTAL PROCEDURE	16
3.1. Magnetron Sputtering Technique	16
3.2. Substrate Selection and Hybrid ITO/Ag/ITO Layer	16
3.3. Overview of Device Structure	18
3.4. Adhesion of Thin Film	19
3.5. Physical Characterization Techniques	20
3.5.1. Measurement of Surface Resistance.....	20
3.5.2. Stylus Method Profilometry	21

3.5.3.	Transmission Measurements	22
3.5.4.	X-ray Diffraction (XRD) Analysis	23
3.5.5.	Optical Microscope Analysis	23
3.5.6.	Scanning Electron Microscopy (SEM) Analysis	24
3.5.7.	Energy Dispersive X-Ray Spectroscopy (EDS) Analysis	24
3.6.	Electrical Characterization	25
3.6.1.	Electro-annealing Process	25
CHAPTER 4.	RESULT AND DISCUSSION	27
4.1.	Tape Adhesion Test Result	27
4.2.	Results of Thin Film Characterization	28
4.2.1.	Sheet Resistance and Thickness Result	28
4.2.2.	Transmission Results	30
4.2.3.	Optical Microscopy Analysis Result	31
4.2.4.	Scanning Electron Microscope (SEM) Analysis Result	32
4.2.5.	Energy Dispersive X-Ray Spectroscopy (EDS) Analysis Result	34
4.2.6.	X-Ray Diffraction Analysis Result	35
4.3.	Result of Electro-annealed ITO/Ag/ITO Layer	37
4.3.1.	Transmission of ITO/Ag/ITO layer after electro-annealing	43
4.3.2.	Band Gap Energy of Grown and Electro-annealed Samples	45
4.3.3.	SEM Images of ITO/Ag/ITO Layer After Electro-annealing	48
4.3.4.	X-Ray Diffraction Analysis Result After Electro-annealing	50
4.3.5.	Variation of Temperature and Time	52
CHAPTER 5.	CONCLUSION	53
REFERENCES	55

LIST OF FIGURES

<u>Figure</u>	<u>Page</u>
Figure 1.1. Graph of transmission and reflection at different energies	2
Figure 1.2. Price distribution of ITO thin film with a magnetron sputtering technique	3
Figure 1.3. Illustration of horizontal distance between target and substrate	5
Figure 2.1. Crystal structure of ITO	12
Figure 2.2. Bixbyite structure with b-site and d-site cations	12
Figure 2.3. Illustration of an n-type semiconductor with an energy scheme.	13
Figure 3.1. System image of deposited hybrid IAI thin films.	18
Figure 3.2. Schematic representation of IAI film structure and electro-annealing. ...	19
Figure 3.3. Schematic diagram of the four-point probe method.	20
Figure 3.4. Illustration of the working principle of a profilometry.	22
Figure 3.5. Bragg's diffraction	23
Figure 3.6. Interaction types between the beam electron and the sample surface.	25
Figure 3.7. The test fixture of electro-annealing system.	26
Figure 3.8. Graph of voltage & time applied to all IAI samples.	26
Figure 4.1. Illustration of applying tape adhesion test before and after the electro-annealing.	27
Figure 4.2. Sheet resistance and thickness of grown IAI thin films.	29
Figure 4.3. The relation between Ag thickness and deposition time.	30
Figure 4.4. Optical transmission spectra of all hybrid ITO/Ag/ITO electrodes.	31
Figure 4.5. Image of using optical microscopy.	31
Figure 4.6. Optical image for different Ag deposited time fixed bottom and top 7 min ITO.	32
Figure 4.7. SEM image of hybrid 7minITO/17sAg/7minITO thin film.	33
Figure 4.8. SEM image of hybrid 7minITO/19sAg/7min ITO thin film.	33
Figure 4.9. SEM image of hybrid 7minITO/21sAg/7 minITO thin film.	33
Figure 4.10. EDS graph of 7minITO/21sAg/7minITO layer.	34
Figure 4.11. EDS graph of 7minITO/19sAg/7minITO layer.	35
Figure 4.12. EDS graph of 7minITO/17sAg/7minITO layer.	35
Figure 4.13. XRD patterns of grown samples with different Ag deposition time.	36

<u>Figure</u>	<u>Page</u>
Figure 4.14. Improvement of sheet resistance after electro-annealing.	41
Figure 4.15. Effect of electro-annealing on transmission value of different samples. ...	43
Figure 4.16. Transmission spectra of grown and electro-annealed samples.	43
Figure 4.17. Transmission spectra of grown and electro-annealed samples.	44
Figure 4.18. Transmission spectra of grown and electro-annealed samples.	44
Figure 4.19. Transmission spectra of grown and electro-annealed samples.	45
Figure 4.20. Graph of absorption coefficient (α^2) versus photon energy (eV) for grown hybrid IAI films with different ITO same Ag thicknesses.	46
Figure 4.21. Graph of absorption coefficient (α^2) versus photon energy (eV) for the electro-annealed hybrid IAI films with different ITO same Ag thick- nesses.	46
Figure 4.22. Graph of absorption coefficient (α^2) versus photon energy (eV) for the grown hybrid IAI films with the same ITO different Ag thicknesses.	47
Figure 4.23. Graph of absorption coefficient (α^2) versus photon energy (eV) for the electro-annealed hybrid IAI films with the same ITO different Ag thicknesses.	48
Figure 4.24. Sem image of hybrid 7minITO/15sAg/7minITO thin film after the electro-annealing.	49
Figure 4.25. Sem image of hybrid 7minITO/17sAg/7min ITO thin film after the electro-annealing.	49
Figure 4.26. XRD patterns of electro-annealed hybrid IAI thin films.	50
Figure 4.27. XRD pattern of samples after the electro-annealing.	51
Figure 4.28. XRD pattern of samples after the electro-annealing.	51
Figure 4.29. Change of temperature versus time electro-annealed hybrid IAI films with different ITO thicknesses.	52
Figure 4.30. Change of temperature versus time electro-annealed hybrid IAI films with different Ag thicknesses.	52

LIST OF TABLES

<u>Table</u>		<u>Page</u>
Table 3.1.	Fixed depositing condition for all hybrid IAI thin films.	17
Table 4.1.	The relation between thickness and deposition time	29
Table 4.2.	EDS result of hybrid ITO/Ag/ITO thin films on borosilicate glass.	34
Table 4.3.	The thickness of the sample in Figure 4.13	36
Table 4.4.	Variation of temperature and current as a function of time.	37
Table 4.5.	Variation of temperature and current as a function of time.	38
Table 4.6.	Variation of temperature and current as a function of time.	39
Table 4.7.	Variation of temperature and current as a function of time.	40
Table 4.8.	Sputtering time parameters and layer properties of IAI film both before and after electro annealing.	42

CHPATER 1

INTRODUCTION

The thesis focused on the electro-annealing model is suggested to increase overall optoelectronic properties of the electrode and including four chapters. In the first chapter, transparent conductive oxide and their derivatives are introduced in terms of their electrical and optical properties with the appearance of growing realization and investigated. The second chapter has been dedicated to literature review of hybrid ITO/Ag/ITO (IAI) transparent electrodes and basics of ITO and its crystal structure theory. In chapter three the overview of the hybrid electrode structure and its characterization technique and indicates improvement of optoelectronic properties by the electro-annealing process has been presented. Finally, chapter four contains the result of experimental analysis in two sections. One of them is results obtained from the films that deposited at room temperature and the other one has improved results with electro-annealing.

1.1. Transparent Conductive Oxides

Transparent conductive oxide (TCO) is a speedily growing area of emphasizing and attention, consolidate an extensive range of research fields. TCO has been an integral part of life due to their vital role as its great electrical conductivity and optical transmittance in different technology especially touch screen technology. Cheap and high quality transparent conductive layers demand like smartphone and its derivative cause to the improvement of effective and novel TCO to response to this demand. In order to figure out the developments in the field of transparent conductive oxides, it is necessary to understand the basic physics in the semiconductors. The large bandgap of semiconductor has been displayed in terms of window transmission in the following Figure 1.1. From the graph, the area optical transparency indicated by b is bounded with allowed electronic bandgap transition at the high energy part another low energy part is bounded by plasma resonance absorption or free carrier electron. The first conducting and transparent thin film which is cadmium oxide is produced in 1907 by Baedeker

(Ederth, 2003). Transparent conductive oxides (TCO) first used in the military field as an anti-icing windshield that was electrically heated in airplanes during world war II. In the early 1950s, research was deepened, and transparent heat-reflective mirrors, antistatic windows, electrical screening applications were added to existing applications.

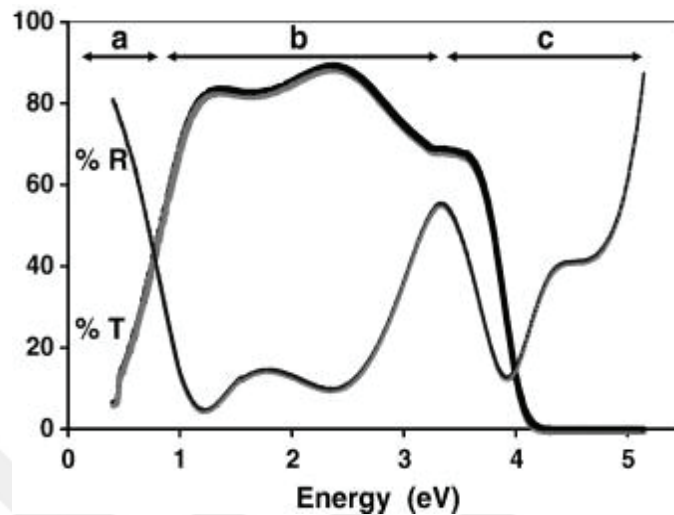


Figure 1.1. Graph of transmission and reflection at different energies (Source: Exarhos and Zhou, 2007).

In the 1960s and early 1970s, transparent conductors started to take part in energy saving applications. Most of these are planar sunlight collectors and low diffusive windows. Recently, transparent conductors have been found wide application areas such as electronics and optoelectronics (Klein, 2000), (Bartella et al., 2001). Most common used transparent conductors are tin oxide (SnO_2), indium oxide (In_2O_3), indium tin oxide (In_2O_3 : Sn or ITO) and zinc oxide (ZnO). As the present time, the most preferred transparent conductive oxide is ITO. Materials present lots of beneficial properties that are ITO to make preferred material. In order to ability easily growth ITO by the precisely controlled thickness and doping concentration lead to the widespread implementations (Barber, 2005). Typical ITO thin film has two chief aspects, its electrical conductivity and optical transparency with a light transmittance of over 85% and conductivity of $10^4 \text{ ohm}^{-1}.\text{cm}^{-1}$ (La, 2017). The trade-off this satisfies different application device requirements. In Figure 1.2, it can be seen that the sputtering target constitutes an essential chunk of the cost approximately 50%. The term transparent conductive oxide (TCO) refers to dense doped oxide semiconductors having a wide bandgap ($\geq 3 \text{ eV}$) to provide light transmittance and high electrical conductivity in the visible region. Due to their high conductivity, these films also exhibit high reflective

properties in the infrared region. Non-stoichiometric and doped tin, indium, cadmium, zinc, tin and their various alloys show high transmittance and near-metal conductivity.



Figure 1.2. Price distribution of ITO thin film with a magnetron sputtering technique.

Diversity of alternative TCOs include indium tin oxide (ITO), aluminum-doped zinc oxide (AZO), fluorine-doped tin oxide (FTO), gallium-doped zinc oxide (GaZO), zinc tin oxide (ZTO) and graphene. This subsection describes an investigation of transparent conductive oxides in terms of optoelectronic properties.

1.1.1. Indium Tin Oxide (ITO) Films

Indium oxide has an amorphous structure before annealing at high temperatures. Sn^{+4} in the structure of the ITO does not interact with In^{+3} at amorphous form so that the mobility and free carrier electron density remain very low stages. In this case, the surface resistivity of ITO is high. Amorphous ITO thin films do not exhibit any x-ray diffraction pattern and crystal structure and it contains a high rate of structural defects which reduce the transparency of ITO thin films that cause optical scattering. The energy bandgap of amorphous ITO films is also low. In other words, the optical transmission of films is low. After the annealing process, ITO thin films gain crystal structure and then the grain size is growing and grain boundary decreases. As a result of these, the optical transmission of the film is increased and large grain size reduces the

surface resistivity of films. In-O bonds are degraded after crystallization, both structural defects are reduced and electron concentration, mobility increased.

1.1.2. Aluminum Doped ZnO Thin Films

ZnO, CdO, SnO₂ and In₂O₃ has been used as a transparent conductive oxide. These binary compounds are easefully doped and controlled to a better transparent conductive electrode. ZnO films are attractive in technological applications due to their optical and electrical properties suitable for optoelectronic devices, gas sensors, light emitting diodes, solar cells, optical fibers. Since ZnO has large forbidden bandgap energy at room temperature. It has a wide range of transparent front contacts in solar cell applications. However, We can see that ZnO films are unstable at high temperatures. Instability of ZnO films supplies a necessity for impurity doped in order to get a good property. ZnO has good thermal stability after doped III group elements

Aluminum-doped zinc oxide (AZO) has been working really hard lately to make transparent conducting electrodes for many application due to low surface resistivity and great optical transmittance performance. Especially, in CZTS solar cells AZO used as a window layer and its mission is front contact also used electron transport layer (Hossain et al., 2016). There are a variety of deposition techniques to prepare AZO thin films. Pulsed Laser Deposition (PLD) (Ou et al., 2011), sol-gel, chemical vapor deposition (Terasako et al., 2007) and magnetron sputtering (Turkoglu et al., 2018) technique are the ones in the literature. Turkoglu et al investigated the effect of substrate rotation speed on the AZO thin film by dc magnetron sputtering method which is represented in Figure 1.3. Among the reasons for preferring AZO for deposition can be shown as resource availability, high chemical stability and their low cost (Fortunato et al., 2008). Characteristic of AZO thin films vary with deposition method and parameters. An overview of the methods of deposition applied in recent time has been fleetingly debated. Al-doped thin film was successfully prepared by Sato H et al using the method of chemical beam deposition with resistivity 3.4×10^{-4} ohm.cm and optical transmittance above 85% in the visible spectrum. Metal-organic chemical vapor deposition has been prevalently used to perform deposition of AZO thin film. B. P. Zhang et al carried out depositing ZnO thin film with the sapphire substrate (Al₂O₃) at different temperature. It is informed that the behavior of crystalline AZO film and its transparency are better at high substrate temperature. Suzuki A et al was succeeded to

deposit AZO film using pulsed laser deposition method utilizing an ArF laser which wavelength is $\lambda=193$ nm. Film transparency is about 90% and their resistivity is $5.62 \times 10^{-4} \Omega \cdot \text{cm}$. On the other hand, the magnetron sputtering technique under the physical vapor deposition method class subheading is generally preferred to prepare AZO thin film.

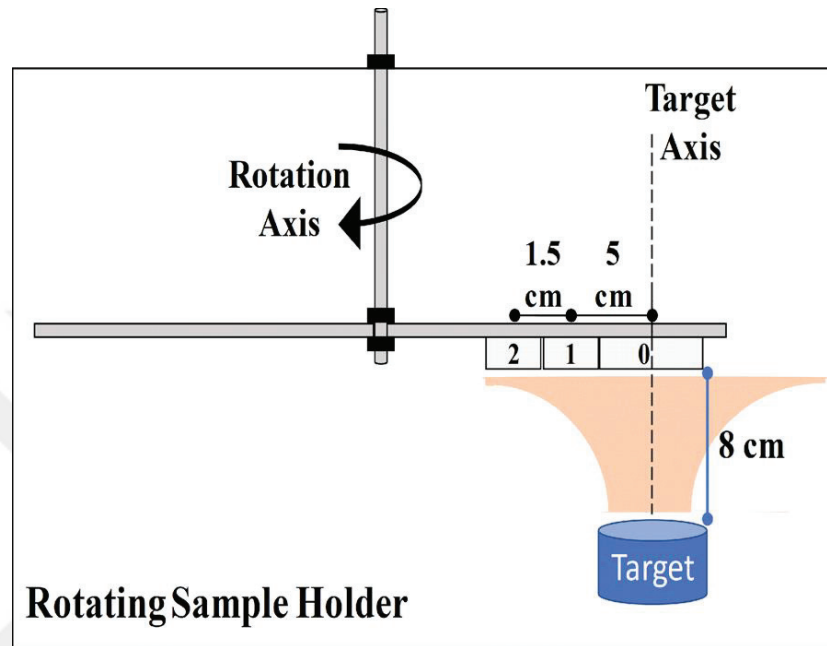


Figure 1.3. Illustration of horizontal distance between target and substrate (Source: Turkoglu et al. 2018).

1.1.3. Fluorine Doped Tin Oxide (FTO) Thin Films

F:SnO₂ is widely prepared as follow by chemical vapor deposition, sputtering and spray pyrolysis. Lattice deformity induced with F doping is minimized against to other cationic dopping likewise Sb, Ta, etc. Because of the anionic radius of fluorine which structure of its similar to O. That's why the rutile crystal structure of SnO₂ which is a tetragonal unit cell shares the same structure with FTO. The principle of FTO unit structure is lightly distorted octahedral. The Sn atom is adapted to the nearest six O atoms. While the thickness of the FTO thin film is increased, grain boundary scattering continuously decreases. If the film thickness of FTO is sufficient, Ionized impurity scattering can be dominated in particular, at great doping concentrations. The bandgap of SnO₂ is about 3.60 eV and have a direct bandgap. Enhancement of F doping cause to raising fermi energy of FTO. The expansion of the bandgap with F doping has generally been observed up to 4 eV (Rakhshani et al., 1998), (Shanthi et al., 1982), (Geoffroy et

al., 1991), (Akkad and Joseph, 2012). Resulting from plasmonic reflection, It can be seen restriction that is about the optical transmission of FTO at the near-infrared region (IR). High reflectivity makes FTO attractive material for heat reflective depositing onto the glass. Transparency of the FTO thin film at visible spectrum is higher than 80% at the same time sheet resistivity is $10 \Omega/\square$ for solar cell utilization. Additionally, it is noted that haze factor is a vital parameter for interperent FTO thin film as a electrode ithe n photovoltaic application. Haze factor the can be defined as the ratio between diffuse transmittance and the total transmittance and depend on the thickness of the surface coating. It is expressed as the fallowing equation, $H(\lambda) = \frac{DT(\lambda)}{TT(\lambda)}$ where $DT(\lambda)$ is diffuse transmittance, $TT(\lambda)$ refers to total transmittance.

1.1.4. Gallium Doped ZnO Thin Films (GaZO)

Gallium has been reported that it is n-type dopants which group III elements (Al-Ga-In) to improve both electrical conductivity and optical transmittance of pure ZnO thin films. Al-doped ZnO based films have certain benefits. The leading advantages are the following low toxicity, increasing chemical stability while decreasing atmosphere pressure, low-cost material and diffusion barrier individuality. On the other hand, Ga doped is increased both humidity resistance and electrical conductivity. If we look doping with two donors, Ga and Al doped zinc oxide thin film exhibits great combination advantageous and enhanced doping efficiency and activation of film. Once and for all, without the requirement of high-temperature doped film exhibit higher crystal quality.

1.1.5. Graphene as a Transparent Conductor

Graphene is an electronic conductive material which is close to perfection in theoretical and experimental terms due to its zero bandgap. The energy of electrons is linearly related to the momentum of electrons at the edges of the Brillouin zone (electrons acts as massless Dirac fermions) and also ballistic transmission is observed in graphene layers. Band structure of graphene was first obtained in 1947 by using the tight-bond model. High electron mobility of graphene can provide broad signal transmission conductivity. Signal transmission conductivity is a vital parameter that determines the gain of an amplifier and the high-frequency performance of the transistor. Carriers in graphene may be both electrons and holes. Conduction band and

valance band of graphene are similar to the funnel and the point where this funnel-shaped valance and conduction band are closest to each other are called dirac point. At these points, the number of electrons and holes is equal to each other. However, due to loads of the carriers are opposite these points are unloaded. Therefore, the Dirac points take the minimum value of conduction. Dirac point is also called a minimum conduction point.

Two-dimensional allotrope of carbon has not been synthesized the fact that of this sent to thought so many researchers at that time. Novoselov and Geim were awarded the Nobel Prize in Physics in 2010 about synthesized graphene using two-dimensional allotrope of carbon. Study of them started with the three-dimensional structure of carbon which is the structure of graphite. Graphite is a layered structure and is formed by bonding two-dimensional graphene crystals with weak van der Waals force. Graphene is an atomic layer of sp^2 hybridized carbon atoms. These atoms are arranged in a hexagonal lattice structure. Graphene exhibits excellent optoelectronic properties. Grafen has been attracted materials due to high carrier mobility at room temperature ($\sim 10\,000\text{ cm}^2\text{V}^{-1}\text{s}^{-1}$), great Young's modulus ($\sim 1\text{TPa}$), extensive specific surface area ($2630\text{ m}^2\text{g}^{-1}$), great optical transparency ($\sim 97.7\%$) and perfect thermal conductivity ($3000\text{--}5000\text{ Wm}^{-1}\text{K}^{-1}$) (Stankovich et al., 2006) (Singh et al., 2011). Recent research has shown that the electronic properties of graphene exceptional. The other unique aspect of graphene appears as the quantum Hall effect in the literature. Graphene has attracted quite an attention depend on physical and chemical properties since the discovery. Considering that a single layer of graphene is 0.42 nm , it is impressive that 30 times stronger than steel. Graphene can provide electric current at light speed due to its high carrier concentration and mobility properties. In other words, the conductor electrons that provide electrical current conduct the current in the material with a speed close to the speed of light, making the graphene more conductive than the known types of materials.

1.1.6. Zinc Tin Oxide (ZTO) Thin Films

The era that we are living in is the electronic age. Almost all people have movable electronic devices. Very few of these people are aware of how these devices work and there are millions of transistors in these devices. Indium-free zinc tin oxide (ZTO) thin film is an n-type semiconductor and It can be seen that a combination of

ZnO and SnO₂ gives ZTO. The mathematical formulation of ZTO can be written as following $(\text{ZnO})_x(\text{SnO}_2)_{1-x}$ here x takes a value between 0 to 1. It is expressed in the literature that Against chemical etching ZTO with $x < 50\%$ is quite stable (Sca et al., 1948). ZTO thin film is a hot topic to applied as a layer making transistor because not so abundant yet largely used indium (Shockley, 1949). Lee et al, indicate that ZTO displays band transport within the saturation regime. Delocalized states are led to band transport. Mobility measurement with temperature dependence is declared that while the temperature is increased, mobility at saturation regime is declined. Propensity shows that it is typically for band transport. ZTO has been deposited by magnetron sputtering, spin-coating, ink-jet printing. ZTO phases are seen in the literature as two phases. One of them is trigonal, ilmenite phase of ZnSnO₃ which seen first time an article of Kovacheva and Petrov in 1998 and applied method was ionic exchange reaction. The other one is the inverse cubic spinel phase of Zn₂SnO₄. This phase reported in 1932 by Barth and Posnjak (Chiang et al., 1977). The main point of ZnSnO₃ phase which is not thermodynamically stable and dissociates into two compounds as Zn₂SnO₄ and SnO₂. The optical band gap of ZnSnO₃ is about 3.50 eV and work function takes value 5.02 eV (Kurz and Aegerter, 2008). conduction band minimum has been described in two phases with empty free 4s and 5s orbitals in order of zinc (Zn) and tin (Sn). Zinc tin oxide as an amorphous oxide n-type semiconductor is provided high-quality device even amorphous phase also ZTO does not contain cost indium.

1.2. Transparent Film Heaters (TFHs)

Transparent film heaters have been used for the application of transparent conductive electrodes and based on Joule heating of the TCE. TFHs are currently an active research area. Heating which is concentrated in only part of the device adverse condition for TFHs based on monolayer ITO and also heating efficiency of ITO is low (Lee et al., 2009).

To address these problems, this dissertation asserts ITO/Ag/ITO hybrid layer. Hybrid layers of ITO/Ag/ITO exhibit great performance for heat generation rate (HGR), uniformity of heat distribution, and thermal response time. The temperature of the heater is determined by the applied gradient of electric potential, the sheet resistivity of thin film and surface heat transfer coefficient for a thin heater of which biot number of the thin heater is quite small. Biot number is the dimensionless quantity and used for a

heat transfer calculation. Heat generation rate (HGR) per area q , the thickness of the TFHs t_f and time operation t , which are determined by the following equations:

$$q = t_f \rho C_p (\partial T / \partial t) = \phi^2 / R_s \quad (1.1)$$

This equation reduces to $q = V^2 / R_s$. Where V is the voltage applied between the electrodes and R_s is the sheet resistance of the sample. TFHs produce more heat for lower R_s value (Langley et al., 2013). Higher film temperature can be attained as the sheet resistivity R_s of TCE is lower when other parameters are fixed. Nonuniform heating of film surface is caused to decrease in the lifetime of the film with forming hot spot (Cheong et al., 2015).

1.3. Electro-Annealing

From the point of classical electromagnetic theory, at the same time occurrence of high apparent transparency and electrical conductivity is nonnormal presented. If number of charge carriers available they make way for high electrical conductivity and heating the charge carriers scatter the incoming electromagnetic radiation. By means of decreasing thickness of films and applying electro-annealing with the idea of quantum theory, the simultaneous occurrence is achievable. Widely used annealing method for transparent conductive oxide is thermal annealing which less effective compared with electro annealing (Kerkache et al., 2006). Thermal annealing has been used for transparent conductive oxides. Electric current well-studied method for amorphous metallic alloy in proportion to thermal annealing (Mizubayashi and Okuda, 1989). Postdeposition electro-annealing is preferable. Because of the fact that technological implementation requires the patterning of thin films. Deposited film at room temperature usually gets result amorphous film that numerous higher etching rate compared with crystalline materials (Rogozin et al., 2006). Local arrangement of the amorphous phase at the beginning of annealing and the following film crystallization is known to cause reducing resistance of thin film (Kim et al., 2011). Increasing the carrier concentration during this process is provided with tin donor activation and oxygen vacancy production. The electro-annealing method is quite effective for increasing the optoelectronic performance of thin films. It can be noted that electro annealing leads to increase work function of multilayer thin films deposited on glass at room temperature. Desired optical and electrical properties of the sample highly depend

on electrical power passing through the film. Electrical performance of the annealed sample is declined when $I > I_{\text{critical}}$ but optical properties are increased. However, both electrical and optical performance is improved with applied $I \leq I_{\text{critical}}$ (Pei et al., 2009). Electrically inhomogeneities in the film which generate locally overheated part are argued as a reason for the acceleration of the crystallization stages (Rogozin et al., 2006).

1.4. Motivation

The main motivation of this research is to achieve high optical transmittance and conductivity with a significant increase on surface resistance of hybrid ITO/Ag/ITO (IAI) thin films by adding conductive silver (Ag) layer between indium tin oxide (ITO) layers, would be provided. Ag was preferred as a metal embedded layer due to having the lowest resistivity among bulk materials. The use of metal Ag between ITOs has improved the electrical and optical properties of the hybrid electrodes, depending on the optimized depositing parameters. The conductivity of the upper layer which is ITO would be mainly investigated depending on the thickness of the Ag intermediate layer. The task of the ITO layers in the stacked hybrid IAI electrode was to increase the overall transmittance in the visible spectral range by reducing the reflection on the metal surface. After the characterization of the hybrid IAI multiple layers, electro-annealing was applied to improve the crystallinity of the films. In this way, hybrid IAI electrodes that high-quality materials will be produced by an electro-annealing method in high optical transmittance and electrical conductivity. Then, the samples were going to be compared between the electro-annealed hybrid IAI films and the IAI three-layer structure, which was not electro-annealing. It is aimed to increase the lifetime of the electronic device by investigating the effect of electrical current on IAI thin films and it will be shown that electro-annealing is a more suitable technique for industrial applications.

CHAPTER 2

THEORETICAL BACKGROUND

This chapter covers the crystal structure of indium tin oxide and the literature review of hybrid ITO/Ag/ITO electrode. In section 2.1 crystal structure of ITO are discussed. In section 2.2 significant electronic level of n-type semiconductors are presented. Eventually, in section 2.3 the chapter is consequenced with the literature review of ITO/Ag/ITO multilayer.

2.1. Indium Oxide and Tin-Doped Indium Oxide

Indium oxide and indium tin oxide has been attracted material among the metal oxides due to electrical conductivity and its optical transmittance. Band theory estimates that it has large band gaps. It has a direct wide bandgap approximately its value is 3.50 eV and classified in the n-type semiconductor.

2.1.1. Crystal Structure of ITO

Structure and composition of ITO make it unique. Indium tin oxide can be achieved by doping Sn^+ to In_2O_3 . Structure of ITO was explained in detail. ITO is a good semiconductor material with high conductivity. Oxygen vacancies or extra metal ions which are at donor sites provided conduction electrons in this film. Chemical reduction or intentional doping is readily created these donor sites. There are two different structure to crystallize of ITO. One of them is body centered cubic the other one is hexagonal.

2.1.2. Body-Centered Cubic Type Structure of ITO

Indium Oxide is crystallized in the Bixbyte Mn_2O_3 type that also the other name is called the c-type rare earth sesquioxide structure. This structure has been known in the literature from the years 1930. At low and normal pressure the phase is acquired. One unit cell of ITO consist of 16 units of In_2O_3 and hence 32 metallic, 48 oxygen atoms located in per unit cell with anion/cation ratio. It means that totally 80 atoms, resulting in instead of complex structure. Model of ITO with two Sn atoms at per unit

cell with 6.25% Sn which are shown in the following Figure 2.1. Indium and Tin atoms are illustrated as big grey and orange balls the oxygen atom is indicated by small red balls.

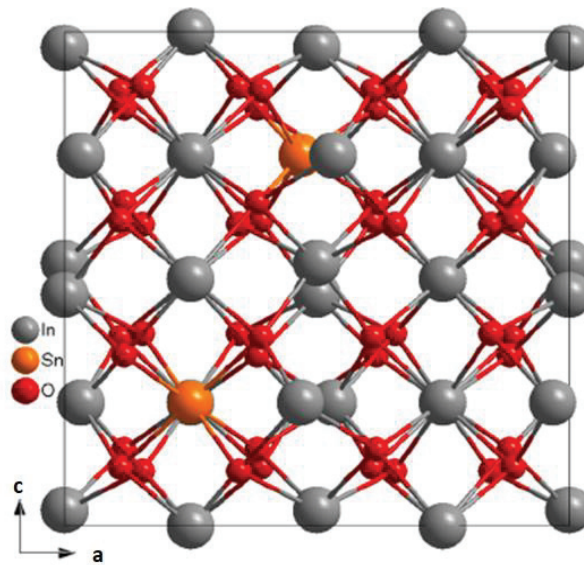


Figure 2.1. Crystal structure of ITO (Source: Lovvik et al., 2014).

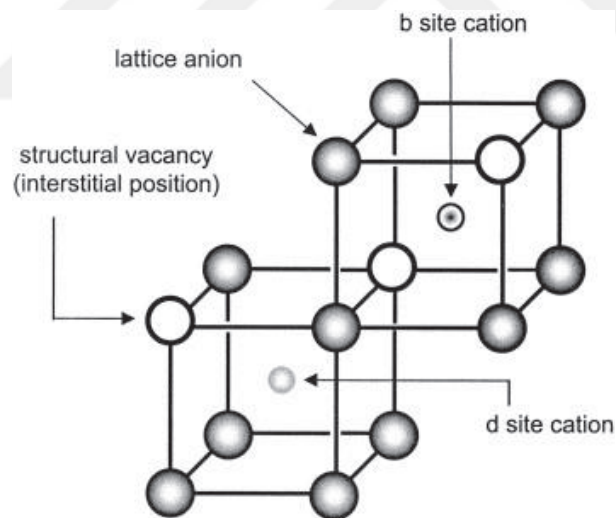


Figure 2.2. Bixbyite structure with b-site and d-site cations (Source: Mason et al., 2002).

Figure 2.2 shows one-fourth of the anions is missing in the structure. Therefore, bixbyite structure can be derived by related fluorite structure. Indium oxide structure contains two type localizations as b-site and d-site. This crystallization type was performed by Marezio in 1965. Throughout the body diagonal that displays in the figure below b-site cations are connected by two structural vacancies, d-site cations are connected by two structural vacancies alongside the face-diagonal. It has been

underlined to noted that structural vacancies are originally oxygen interstitial positions. Parameter of the lattice is reported 10.12 Å.

2.2. Significant Electronic Levels

Materials can be identified as semiconductor when its electrical resistivity measured at room temperature throughout between from 10^0 and 10^{11} Ωcm. Introducing the energy to a system that energy over the value of bandgap, electrons excited from fully occupied valance band to the empty conduction band. The positively charged hole is formed in the valance band during this process. Electrons and holes can cause to an enhancement in conductivity after applied voltage. However, the band structure alone is not enough to characterize semiconductors.

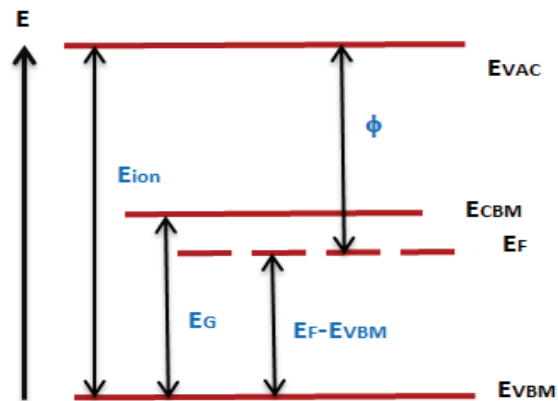


Figure 2.3. Illustration of an n-type semiconductor with an energy scheme.

Figure 2.3 shows that work function (ϕ) is obtained by the potential energy difference of an electron between Fermi level (E_F) and vacuum level E_{VAC} . The work function of Indium tin oxide takes the value of 4.60 eV (Brown et al., 1992). The work function of clean 111 silver surface is approximate to 4.74 eV is express in the literature (Farnsworth and Winch, 1940), (Dweydari and Mee, 1973). Extracting an electron from valance band to the vacuum level is provided by ionization energy.

Ignition contact: In general terms, it is considered that two material come into touch with the least resistance (ideally zero). The contact surfaces should be clean, smooth and bright in order to get an ideal contact. When the two materials are brought into contact, a new charge distribution occurs between them. In such a system, the Fermi

energy levels of both materials are the same as a result of the thermal equilibrium. This is the case between the two metals, It may also be in the contacts between metal and n-type or p-type semiconductors. The physical properties of the charge and potential distributions of the ohmic and rectifier contacts and the current transmission phenomenon play an important role in solid-state electronics. We can define the parameters that determine the properties of a contact.

Work function (Φ): The amount of energy required to remove an electron from the Fermi level of the metal or semiconductor to the surface by zero kinetic energy.

The electron affinity of the semiconductor (χ): the energy difference between the lowest energy level of the conduction band and the vacuum level.

2.3. Literature Review: Hybrid ITO/Ag/ITO Layer

There are limited studies investigating the effects of electro annealing on hybrid IAI thin film properties. The surface resistivity of the IAI multiple layers varies with the Ag layer deposited time (Hong et al., 2012). While the thickness of the Ag layer increases, rapid increment in electron density, as well as a decrease in electron mobility, is observed. Hall mobility of IAI hybrid film decreased with increased carrier concentration as in consequence of ionized impurity dispersion. Resistivity depends on the parameters which are shown in Equation 2.1,

$$\rho = \frac{1}{\sigma ne\mu} \quad (2.1)$$

Where ρ denotes resistivity, σ , electrical conductivity, n , carrier density, e , electronic charge and μ , hall mobility. The resistivity of the hybrid layer arrestingly improved because of the fact that the increase of n was larger than the decrease of μ . With an increase in the thickness of Ag metal in the hybrid layers, n and μ scaled up. This appearance could arise from an increase in free electrons per unit volume. In other respects, hall mobility μ of IAI film increased as the embedded Ag layer thickness is increased. This action is ascribed to transition from the formation of the island to continuous film. All these results show to us electrical conductivity σ is affected by Ag interlayer (Cheng and Ting, 2007). There is so many research paper in the literature about decreasing surface resistivity of ITO monolayer. Decreasing surface resistance value requires a high-temperature process. However, hybrid IAI layers deposited at

room temperature exhibit great conductivity without an extra difficult process (Song et al., 1999). When the oxygen gas flow rate increases optical transmission of the films decreases (Demirhan et al., 2019). Discontinuity on film, agglomeration of the embedded Ag layer in the interface region of the IAI multilayer thin film and the diffusion of the oxygen layers along the crystalline ITO grain boundaries into the Ag layers results in the electrical and optical degradation of the IAI thin film. If the Ag grains are bound to the lower ITO layer, the IAI films can perform electrical and optical performance with excellent correlation. Auger electron spectroscopy depth profile for hybrid IAI electrodes revealed that there was no interfacial reaction between metal Ag and ITO layers due to the high formation (Jeong et al., 2009). Increasing the annealing temperature cause to reducing the surface resistivity and rising the optical transmittance (Tuna et al., 2010). This may be due to the improvement in IAI multiple layer crystallinity and the reduction of Ag's absorption coefficient close to UV (Lee et al., 2013). As the temperature of the electro-annealed IAI thin films increased, some of the crystal phases increased and their orientation appeared in plane 400 (Koseoglu et al., 2015). Annealing is a process for obtaining a low energy state of a solid. The process contains mainly 2 steps. One of them is increased the temperature of the heat to a maximum value at which the solid melted. The other one has decreased the temperature carefully until the particle arranged themselves in the ground state which is minimum energy state. The ground energy state is obtained only if the maximum temperature is high enough and the cooling is done slowly.

CHAPTER 3

EXPERIMENTAL PROCEDURE

The essential purpose of this research is to the growth of hybrid ITO/Ag/ITO thin film on borosilicate glass. Investigate its structural, electrical and optical properties and then perform electro-annealing in the air to improve properties of the electrode. In this section, the study was divided into two main parts. The main study is deposited hybrid ITO/Ag/ITO layer on borosilicate glass at room temperature under high vacuum. The second part of the study was continued as after the examination of optical and electrical properties of deposited films, electro-annealing was applied to the sample and effect of electro-annealing was investigated on the improvement of overall transmission and electrical properties.

3.1. Magnetron Sputtering Technique

In this part, the deposition method of hybrid IAI thin films was explained. Magnetron sputtering technique was preferred to the production of IAI films due to their lots of benefits, Uniformity is one of the certain advantages of magnetron sputtering technique. The other primary advantages of sputtering are large deposition rate, easy of depositing metal or alloy or compound, adhesion of film is also extremely high. Heat sensitive substrate depositing can be performed (Swann, 1988). Large area substrate was easily deposited with great uniformity by magnetron sputtering system (Koseoglu et al., 2015). Basically, the principle of magnetron sputtering technique is bombarding the target with energetic ions, target's surface atoms are ejected and these ejected atoms from target are condensed on the substrate surface.

3.2. Substrate Selection and Hybrid ITO/Ag/ITO Layer

In this dissertation, non-alkaline borosilicate glass was used as a substrate due to lower thermal expansion coefficient ($\sim 3 \times 10^{-6} \text{ K}^{-1}$ at $20 \text{ }^\circ\text{C}$) and high resistance to thermal shock. Compare with standard soda lime glass it can withstand thermal reaction and high pressure. It also provides high optical transmission and clarity. It is widely

used as a reinforcement in composite material, thermal insulation material and PCB in the various industry. These reasons make it ideal to ensure IAI films quality and multitalented glass material.

All IAI thin films were deposited by dc magnetron sputtering at room temperature. Chamber is evacuated to a base pressure of 5×10^{-6} Torr only prior to deposition. Then inert gas (generally used Ar gas) is introduced the vacuum chamber. Dc potential was applied to between cathode and anode to created plasma which contains free electron and moving charged particles. The cathode is referred to as target material, the anode is referred to as the substrate. Before deposition to get contamination free ITO and Ag target surface 5 minutes pre-sputtering was performed. IAI thin films were deposited Ar atmosphere at room temperature with constant power. Substrate holder was rotated to improve the uniformity of hybrid film and connected to dc motor. LabView design program controls both shutter and substrate holder. In order to deposit the metal Ag layer in as short as 13, 15, 17, 19, 21 seconds, using the LabView program rather than turning the shutter manually, more precise results were obtained. DC magnetron sputtering system which is used for this deposition has illustrated in Figure 3.1.

Table 3.1. Fixed depositing condition for all hybrid IAI thin films.

Deposition Parameters	Value
Power (Watt)	15 W
Sputtering gas	Ar
Ar flow rate (sccm)	40 sccm
Base pressure (Torr)	5×10^{-6} Torr
Working pressure (mTorr)	3×10^{-3} Torr
Substrate size	$3.5 \times 2.5 \text{ cm}^2$
Substrate temperature	Room temperature

Thickness value of films was optimized. Optimized condition for hybrid IAI layers was showed in Table 3.1. To get the desired and exact thickness step creation method was preferred and used. Dektak surface Profilometer was used for thickness optimization. Before samples were placed in the system small drop of AZ5214 photoresist was dropped on calibration glass. After the samples are removed from the system, resist was remove by using acetone with ultrasonic bath. Result of these work,

step creation was obtained. Thickness measurement result was given in the result section.

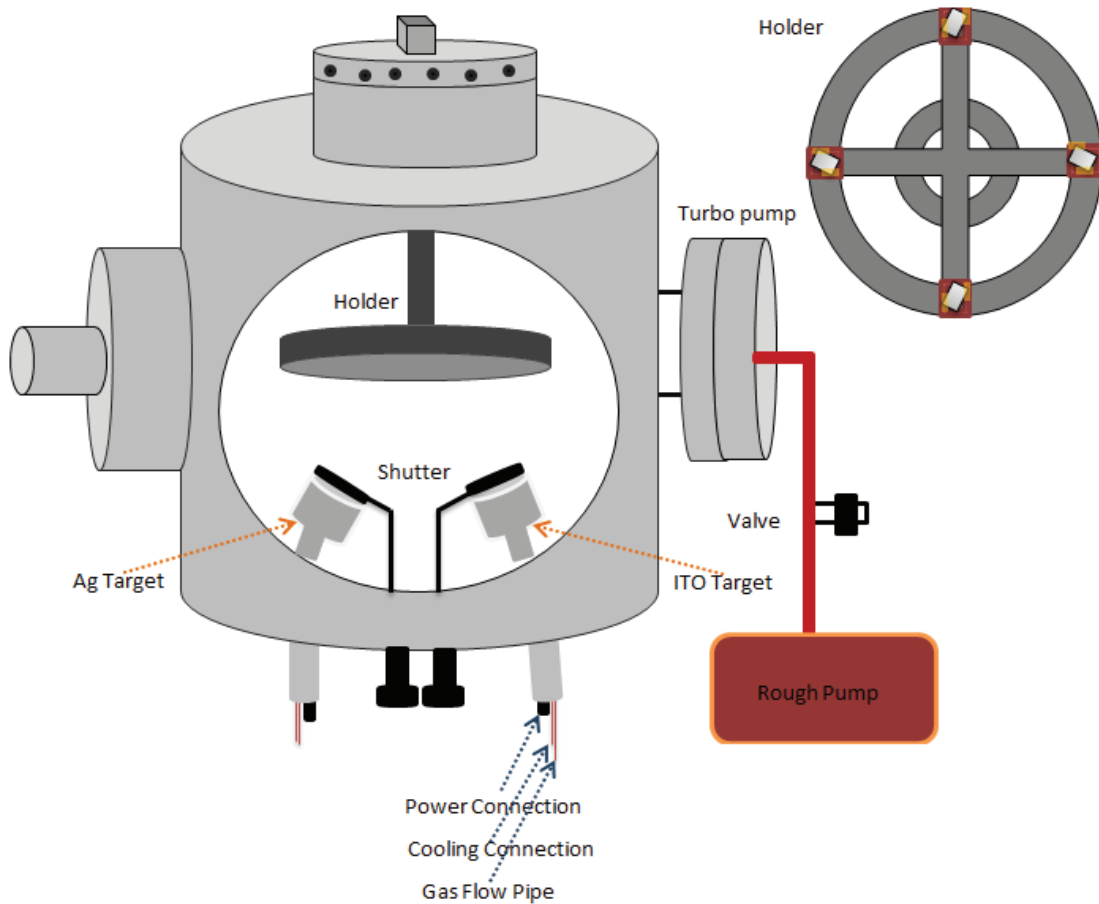


Figure 3.1. System image of deposited hybrid IAI thin films.

3.3. Overview of Device Structure

In this contention, the IAI layers were deposited by dc sputtering of ITO and Ag onto borosilicate glass at Ar atmosphere without breaking vacuum at room temperature.

1. Borosilicate glass which has high chemical durability was used as a substrate.
2. The substrate was cleaned in an ultrasonic bath in the order of acetone, methanol, propanol and de-ionized water for each step about 10 minutes. The final step is plasma etching for 10 min to remove organic residue from the substrate.
3. ITO (purity of 99.99%, weight percent of 10-90 for SnO_2 and In_2O_3) and Ag (purity of 99.99%) were used as a target.

4. Target to substrate distance was kept at 7.2 cm for each deposition
5. The sample holder was controlled and adjustment via LabView design program in order to obtain homogeneous distribution on the film,
6. Ar gases introduced the vacuum chamber before the starting deposition.
7. ITO and Ag's target were pre-sputtered at 5 minutes respectively.
8. Sputtering was performed with various ITO and Ag deposition time parameter.
9. Electro-annealed was applied to the obtained sample in an air environment.
10. After all step, the desired structure was obtained as shown in Figure 3.2.

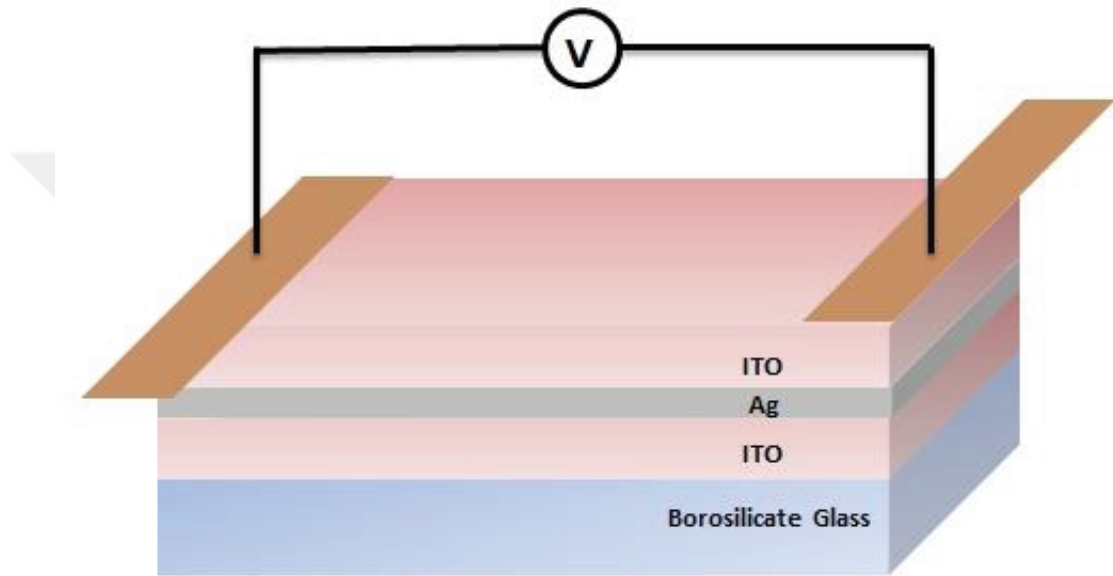


Figure 3.2. Schematic representation of hybrid IAI film structure and electro-annealing.

3.4. Adhesion of Thin Film

The most basic feature expected from a coating is that adhesion between the coating and the substrate material is acceptable and sufficient at any application. Because the chemical, physical, mechanical and tribological properties of the coating are significantly affected by the adhesion properties of the coating. According to the American Society for Testing and Materials (ASTM) D907-70 standard that adhesion express as “the state in which two surfaces are held together interfacial forces may consist of valance forces or interlocking forces or both” (ASTM-D907-70). These bonding forces can be expressed as van der Waals, electrostatic or chemical bonds which occurs at the interface formed by the interfacial surfaces. There are different approaches to identify and classify adhesion. The widely accepted approaches were

exhibited by Mittal and adhesion was categorized as 2 classes. Adhesion is occurred due to the force acting on the coating and substrate system.

3.5. Physical Characterization Techniques

In this subsection physical characterization was explained in detail.

3.5.1. Measurement of Surface Resistance

Surface resistance is commonly used to define the resistance of thin films with a unit of ohms/square. The working principle in the background of the four-point probe device is illustrated in Figure 3.3.

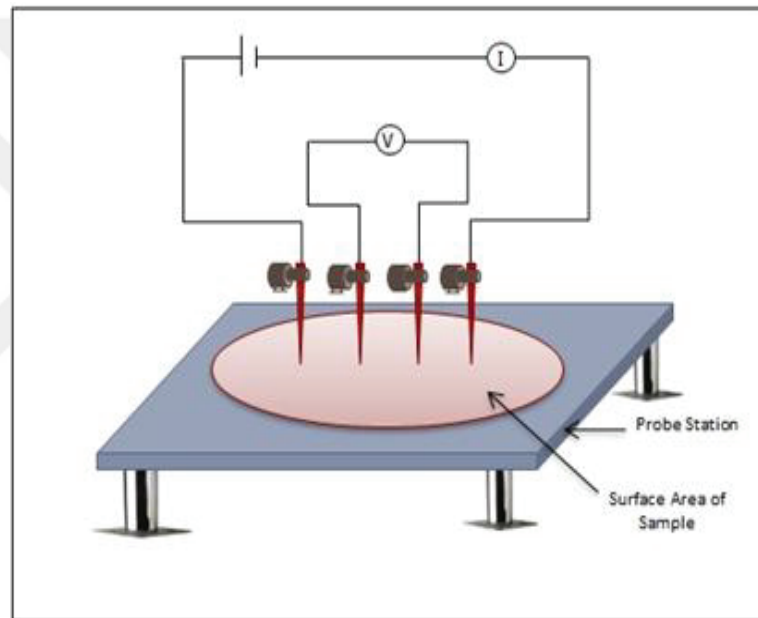


Figure 3.3. Schematic diagram of the four-point probe method.

The two outer probes are connected to the Keithley model constant current source, the other two inner probe record the drop in voltage to get the potential difference. The current source is programmed to the desired current output and the current in a finite plate indicates a logarithmic increasing potential. The electrostatic analysis of the distribution of the electrical potential and area in the film gives the equation $R_s = \alpha V / I$. Where α is a constant and its value equals to 4.5324 which varies depending on space and configuration of the contacts. Thus, the surface resistivity of the measured sample is calculated as $R_s = 4.5324 V/I$. Theory of four-point probe was explained in the next paragraph.

For a thin film sample, the thickness is smaller than the spacing between the probe ($t \ll s$) case of the current ring is essential.

$$A = 2\pi xt \quad (3.1)$$

$$R = \int_{x_1}^{x_2} \rho \frac{dx}{2\pi xt} = \int_s^{2s} \rho \frac{dx}{2\pi xt} = \frac{\rho}{2\pi t} (\ln x) \Big|_s^{2s} = \frac{\rho}{2\pi t} \ln 2 \quad (3.2)$$

Superposition of current at outer two tips cause to $R = V/2I$, Therefore, the sheet resistivity of a thin film specimen is

$$\rho = \frac{\pi t}{\ln 2} \left(\frac{V}{I} \right) \quad (3.3)$$

$$R_s = \frac{\rho}{t} \propto \left(\frac{V}{I} \right) \quad (3.4)$$

$$\alpha = \pi / \ln 2$$

$$\ln 2 = 0.693 \dots$$

and hence, sheet resistivity takes the simple form,

$$R_s = 4.53 (V/I) \quad (3.5)$$

3.5.2. Stylus Method Profilometry

Profilometer actuated with the electromechanical system. Electromechanical system which is in control of mechanical systems with the electronic system does not contain software. Aim of the stylus method is to trace the topography of a film-substrate step. The working principle in the background of the device is shown in Figure 3.4. The stylus is acted with a fixed velocity and force through the layer. There is a tip which is made of diamond on the top of the stylus with a radius of approximately $10 \mu\text{m}$. The force of stylus is adjustable from 1 to 30 mg. Vertical deviation of the stylus is measured through the instrument of Linear Variable Differential Transformer (LVDT) sensor. As a consequence, the height profile results obtained. Height of the resulting step-contour trace shows directly film thickness. There are several restrictions about the accuracy of stylus-model such as stretching and penetration of film, substrate roughness and vibration of the equipment. Substrate roughness introduces extravagant noise into measurement, which creates uncertainty in the position of the step (Milton Ohric, 1992).

In this thesis, all deposited sample thickness were determined stylus method and using Veeco DEKTAK 150 Profilometer.

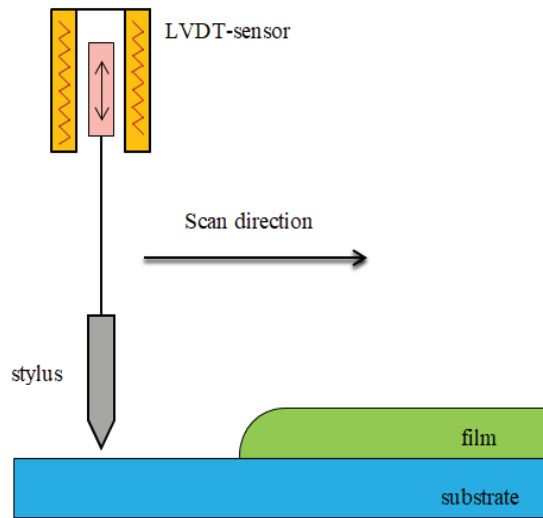


Figure 3.4. Illustration of the working principle of a profilometry.

3.5.3. Transmission Measurements

Transmittance-wavelength spectra of optical thin films can be divided into three parts. The desired and required transmission value is obtained in the short wavelength absorption edge which is dependent on the electronic structure of the material and between the long-wavelength limit. The characteristic of the transparent region depends to a large extent on the material itself, in particular, the stoichiometry and impurity of the material causing the absorption. The transparency of thin films is usually slightly less than that of the substrate material and it is largely associated with growth conditions. A slight deviation in stoichiometry or actual absorption due to contamination is the cause of the increase in the damping coefficient of film. Other reasons include surface roughness, inner grain boundary, density fluctuation due to the crystal structure, microstructure, fine holes, cracks and similar reasons (Danielzik et al., 2003). The spectrophotometer is fastest method among interference systems to obtain the optical properties of the films in visible and near IR spectral regions, These films generally have a thickness of 100 nm and their spectra give an advanced pattern of interference.

3.5.4. X-ray Diffraction (XRD) Analysis

The purpose of XRD measurement is to identify the crystal structure of hybrid IAI thin film. It can determine the internal strain and crystallite size of material and XRD gives information about the quality of the film. Scherrer's equation is the estimated average of crystallite size and calculated with the following Equation 3.6,

$$L = \frac{k\lambda}{\beta \cos\theta} \quad (3.6)$$

λ is the wavelength of X-ray source with a unit of nanometers. Constant which is k related to the crystallite shape which taken as 0.89. β is the full width of half maximum the diffraction peak at half maximum height (FWHM) in unit radians and θ refers to Bragg's diffraction angle which is shown in Figure 3.5 (Monshi et al., 2012).

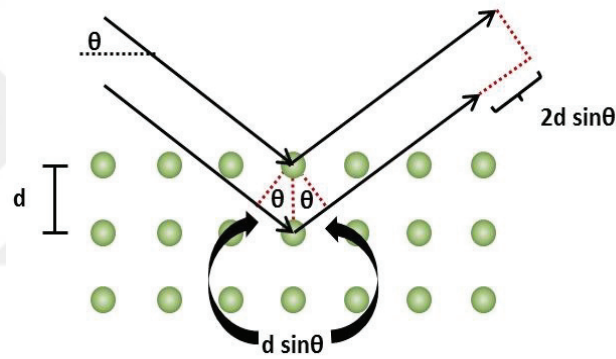


Figure 3.5. Bragg's diffraction (Source: Anton Paar Wiki).

Bragg-Brentano diffractometer configuration that on the Philips X'Pert Pro X-ray diffractometer was used for XRD measurements. Bragg's diffraction law illustrated as the following Equation 3.7,

$$2d\sin\theta=n\lambda \quad (3.7)$$

where d is the plane spacing, θ is the diffraction angle, n is an integer and λ is the incident wavelength.

3.5.5. Optical Microscope Analysis

It can be constitutively categorized optical microscopy system under six main heading. Based on their kind of utilization area brightfield optical microscopy, darkfield

microscopy, oblique illumination, phase contrast light microscopy, differential interference contrast microscopy, confocal laser scanning have emerged.

3.5.6. Scanning Electron Microscopy (SEM) Analysis

Surface morphologies of hybrid ITO/Ag/ITO layer which was deposited with introducing 40 sccm Ar rate at room temperature with various deposited Ag time were analyzed by SEM. How it works will be explained in a simplistic way referring to Skoog and Leary's book. There is 3 main part of the scanning electron microscope. The first part is the electron gun. After electron gun part secondly focusing part appears. Finally, the third part is the sample chamber which is contained in the sample. All three part is kept under ultra-high vacuum (UHV). The energy of a motionless electron outside the metal defines as a vacuum level. In an electron gun, electron beam produced and accelerated. Electromagnetic lenses that are contained in the second part makes to electron gun condensed and focused. Lastly, the specimen surface has been scanned by the electron beam and their signals are collected by the detector. Metallic filament, Wehnelt cylinder, and anode are part of the electron gun. Electron gun source is generally as a tungsten, Lanthanum hexaboride (LaB₆) and field emission gun (FEG - ZrO/W). In order to create a free electron, these guns heated nearly up to melting points. Obtained free electron accelerated towards to anode part. Transportation is supplied by an applied voltage up to a maximum of 50 kV. Wehnelt cylinder which has a negatively charged is blocked the electron which has a small velocity. The only fastest electron can pass from the Wehnelt cylinder. Topological information is obtained as a function of x-y direction scanning. When the electron hits the specimen surface, many interactions can occur. Resulting in inelastic scattering, the secondary electron emerges depth between 0.5 nm to 5 nm. Due to the energy transfer, specimen electrons leave the sample if gained enough energy. Interaction volume depends on the acceleration voltage and the atomic number of the specimen.

3.5.7. Energy Dispersive X-Ray Spectroscopy (EDS) Analysis

EDS measurements which are a tool of qualitative and quantitative examination of the specimen were obtained by BSD detector. The energy of the electron specifies the depth of the region where the X-ray comes from the specimen. Interaction kinds

between the electron beam and specimen are shown in Figure 3.6. depend on the incident energy of the beam.

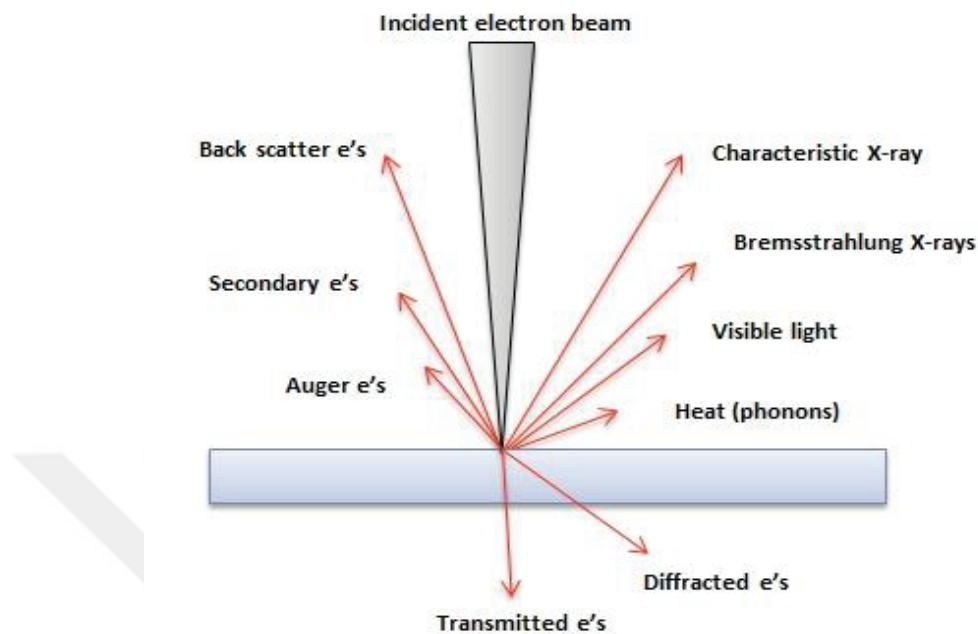


Figure 3.6. Interaction types between the beam electron and the sample surface.

3.6. Electrical Characterization

Electro-annealing was applied to improve the optoelectronic performance of the hybrid electrode. This subsection includes electro-annealing process and fixed graph of the applied voltage to all samples.

3.6.1. Electro-annealing Process

The fabricated multilayer IAI electrodes which deposited at room temperature was amorphous phase The steps we have taken to apply electro-annealing to the improvement of film crystallinity are as follows,

1. The copper plate was cut in the form of a thin strip (1 μm thick, 5 mm wide, 3 cm length) and was attached two opposite edges of the substrate with clamps to apply a constant current.
2. The n-type thermocouple was placed on the corner side of the film to controlled the electro-annealing temperature.

3. Measurements were performed by connecting to external power supply and multimeter to read constant AC voltage. Figure 3.7 shows the test fixture of electro annealing system.

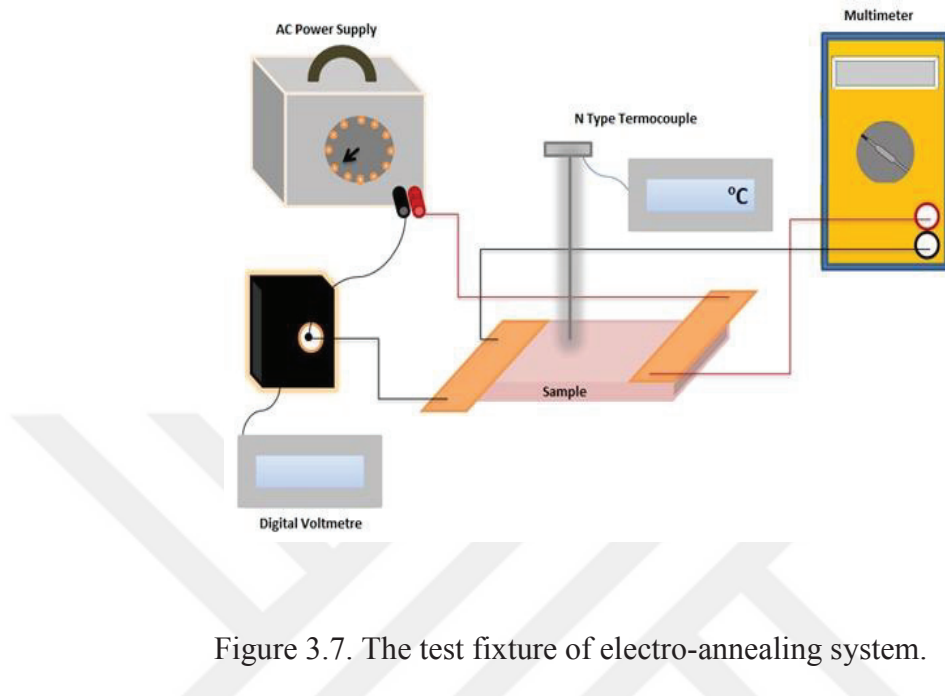


Figure 3.7. The test fixture of electro-annealing system.

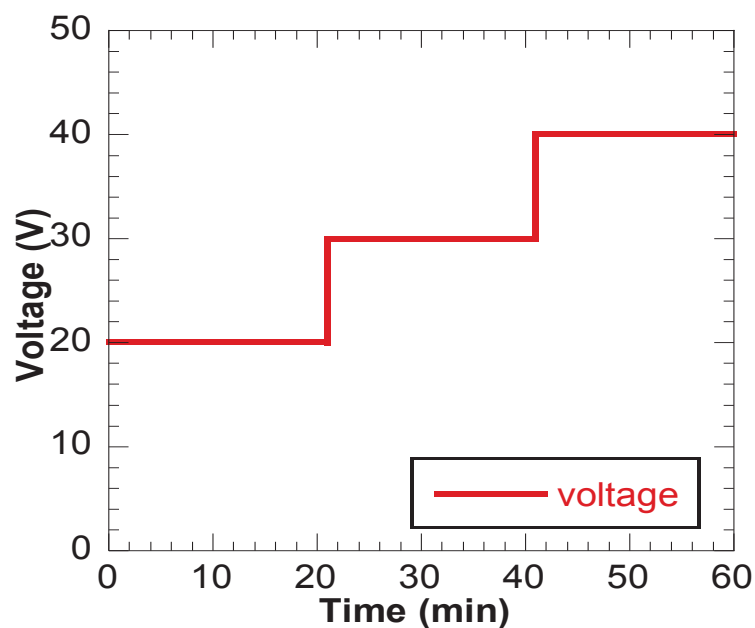


Figure 3.8. Graph of voltage and time applied to all IAI samples.

4. Electro-annealing was performed to each sample by adjusting AC power supply manually 20, 30, 40 AC Volt during 20 minutes respectively. Effect of electric current on the IAI layer without breaking voltage was investigated. Figure 3.8 shows a graph of the applied voltage to all sample as a function of time.

CHAPTER 4

RESULT AND DISCUSSION

In this section, the result of the investigation would be illustrated divided into 2 sections and discussed. The initial section deals with the investigation of the hybrid layer which deposited room temperature and shows outcome from the thin film characterization. In the following contention discusses the result of the electro-annealing effect and gives information about the improvement of electrical and optical properties.

4.1. Tape Adhesion Test Result

Tape adhesion test applied to measure the degree of adhesion of the depositing film to the layer.



Figure 4.1. Illustration of applying tape adhesion test before and after the electro-annealing.

Performance of adhesion is controlled by adhering tape and immediately pulling away in order to decide whether the depositing comes off and as it does, to how much. Mechanical exfoliation is defined basic peeling process that applied without heated IAI hybrid layer. Scotch tape is applied to the surface, therefore exerts a normal force. The exfoliation mechanics are dominated by a normal force. Dispersion of the film is taking place in the adhesive. Illustration of the peeling process shown in Figure 4.1 The substrate

borosilicate glass in the image was deposited at room temperature, without heating film easily peeling from the substrate surface. After electro-annealing coating film was showed better adhesion to borosilicate substrate.

4.1.1. Results of Thin Film Characterization

In this section, thin film characterization results are illustrated and discussed. Surface resistivity was measured with a Keithley 2424 instrument. Optical properties of IAI thin films were measured by spectrophotometer. It's type PerkinElmerLambda 950 UV/Vis/NIR Spectrophotometer from 2600 to 200 nm. Information about the morphology of hybrid IAI thin film was carried by Nikon ECLIPSE LV 150 optical microscope and scanning electron microscope (SEM). Elemental composition of the specimen was analyzed with energy-dispersive X-ray spectroscopy (EDS). XRD results catch out the nanocrystalline structure of IAI film.

4.1.2. Sheet Resistance and Thickness Result

The sheet resistance of ITO monolayer was 142.61 Ω/\square . For the hybrid ITO/Ag/ITO layers 16.87, 13.58, 11.54 and 9.05 Ω/\square for the silver sputtering time of 15, 17, 19 and 21s, respectively. Figure 4.2 shows the sheet resistance of the hybrid layers was noticeably reduced when compared to the ITO monolayer. The sheet resistance of hybrid IAI layers decreased with increasing silver thickness. Top and bottom layer ITO in the hybrid structure is deposited 7 minutes. The embedded metal Ag resistivity can be calculated as the given formula,

$$\rho_{Ag} = t_{Ag} \left(\frac{1}{RSq} - 2 \frac{t_{ITO}}{\rho_{ITO}} \right) \quad (4.1)$$

In this equation ρ_{Ag} is the resistivity, t_{Ag} is the thickness of the metal Ag and RSq is the sheet resistivity of the hybrid layer. t_{ITO} is the thickness, ρ_{ITO} is the resistivity ITO layer. The resistivity of the top and bottom layer ITO in the hybrid structure is assumed to be constant. Based on the experimental result of Figure 4.3 optimizations were made.

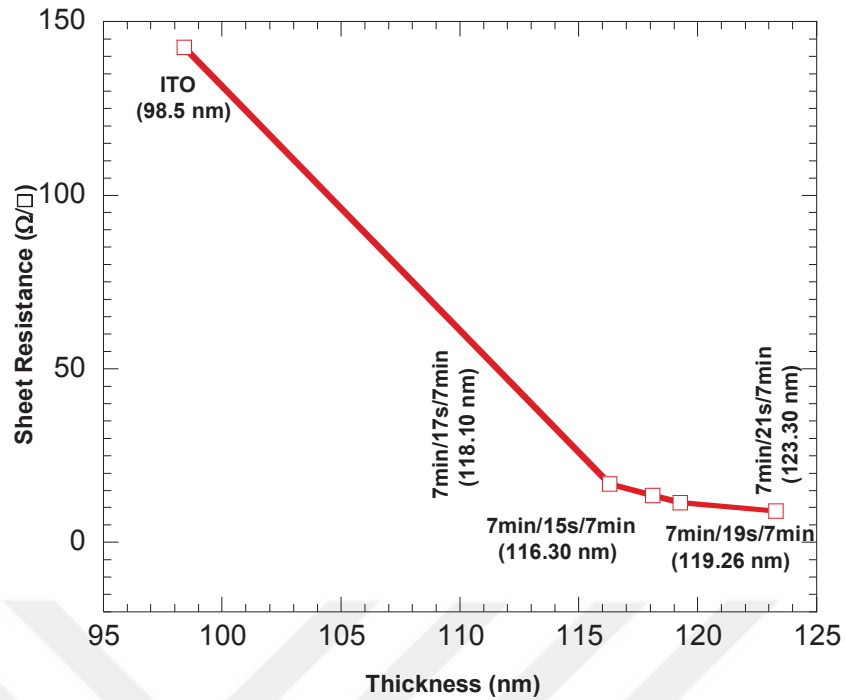


Figure 4.2. Sheet resistance & thickness of grown IAI thin films.

Table 4.1. The relation between thickness and deposition time

Sputtering Time (s)	The Thickness of Ag (nm)
10	10.6
15	12.4
20	12.9
25	14.2
30	16.6
40	17.9

Table 4.1 shows the relationship between silver thickness and sputtering time. Silver metal deposited between two ITO because of its lowest resistivity between bulk materials. The resistivity of silver is $1.59 \times 10^{-8} \Omega m$. Silver cannot resist the flow of electrons very well. Because resistivity is inversely proportional to the conductivity. The silver between the two ITO layers is not oxidized. The reason for this that deposition is carried under Ar atmosphere without breaking the vacuum. It has a high electrical and thermal conductivity because of their single s electron is free and so does not interact with the filled d subshell.

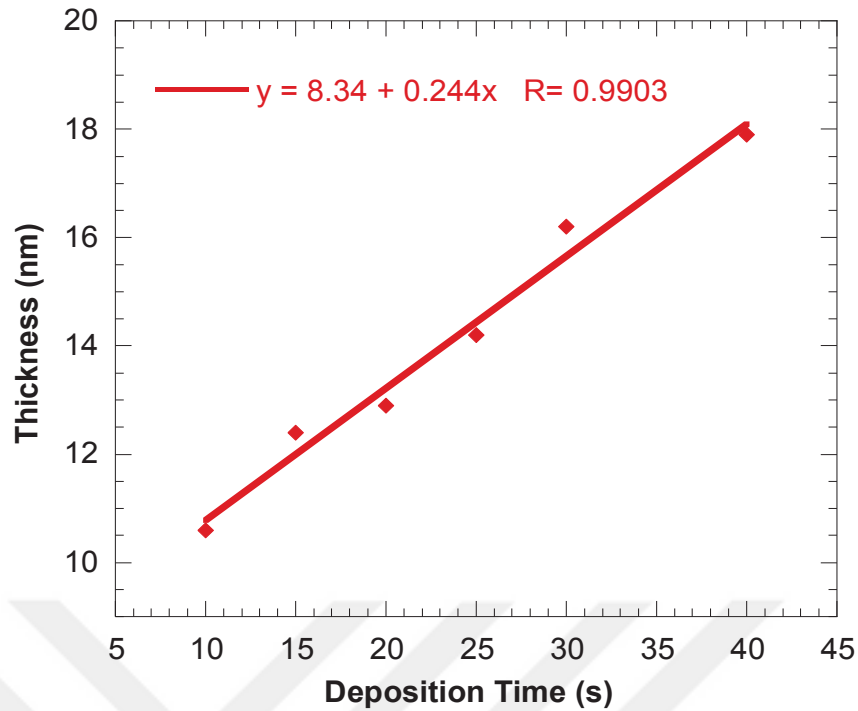


Figure 4.3: The relation between Ag thickness and deposition time.

4.1.3. Transmission Results

The deposited of ITO with low resistivity and high optical transmittance needs to the requirement of elevated temperature about 260 °C and needs post-annealing over 300 °C. However, while inserting a thin metal Ag layer between that ITOs optical transmittance results similar to that ITO is achieved with low resistivity. Great optical transmittance of hybrid IAI layers in the visible spectrum is due to the antireflection effect. ITOs with the finite thickness that dielectric layers neutralized the reflection from the Ag layer (Sibin et al., 2017). It is observed that increased deposition time of metal Ag when ITO is fixed led to lower optical transmittance. Old studies have shown that lower thickness of Ag layer indicates island structure as Wolmer Weber growth mode rather than continuous film (Wang et al., 2006). The Ag layer should be thin, continuous and uniform for high transparency, Due to light scattering, isolated islands, which are formed when depositing the Ag layer, reduce optical transparency. Optical transmittance results show without electro-annealing process achieving maximum transmittance was 88.7% at $\lambda=552$ nm. Figure 4.4 displays total transmittance of hybrid IAI/borosilicate glass of diversified Ag layer thicknesses.

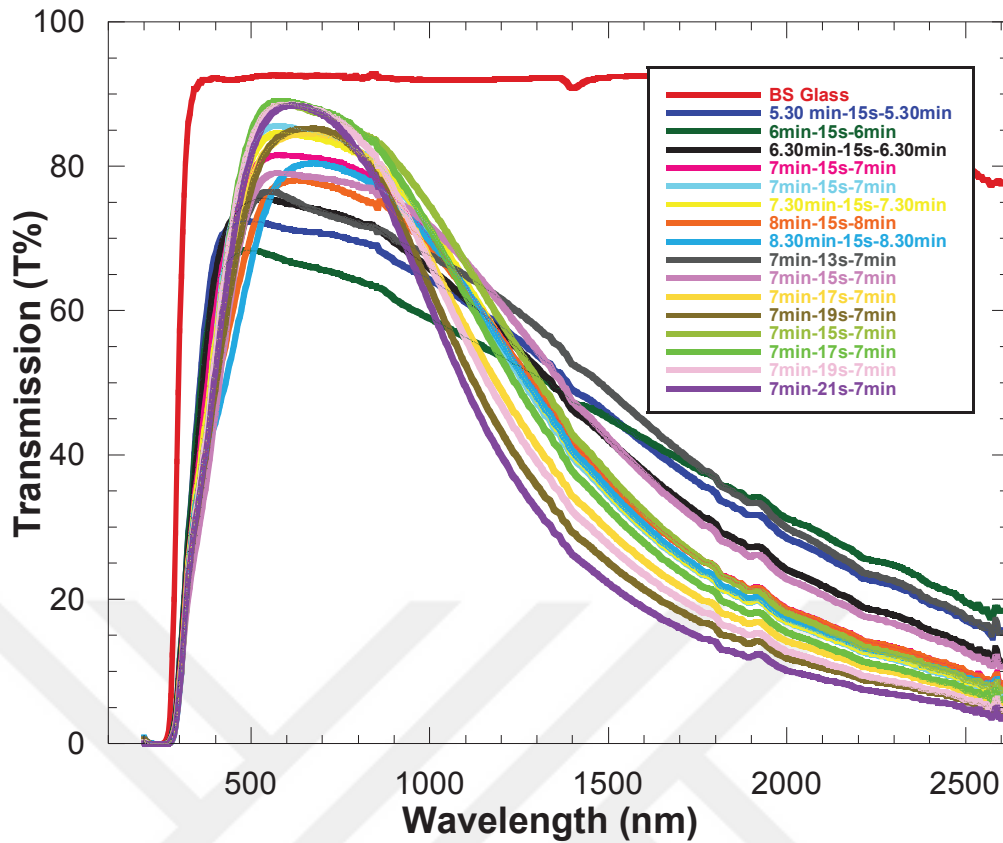


Figure 4.4. Optical transmission spectra of all hybrid ITO/Ag/ITO electrodes.

4.1.4. Optical Microscopy Analysis Result

Nikon ECLIPSE LV 150 optical microscope shown in Figure 4.5 was performed to analysis homogeneity and roughness of hybrid IAI thin film surface. It was a class 10.000 cleanroom in the Physics Department of IZTECH.



Figure 4.5. Image of using optical microscopy.

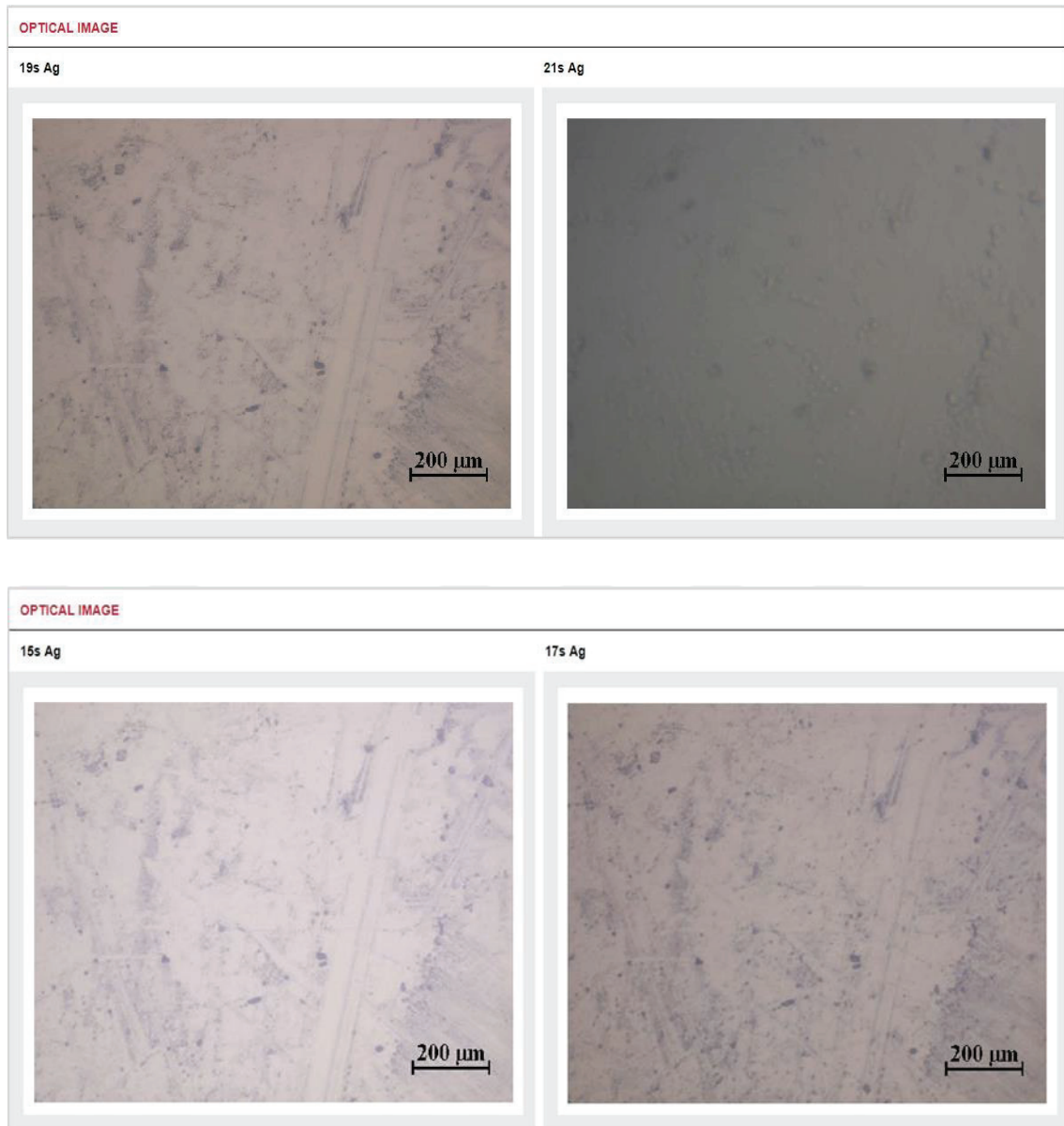


Figure 4.6. Optical image for different Ag deposited time fixed bottom and top 7 min ITO.

Figure 4.6 shows clearly deposition parameters were the vital effect on roughness surface. To attain the definite result scanning electron microscopy (SEM) images were performed.

4.1.5. Scanning Electron Microscope (SEM) Analysis Result

Top view surface analysis was performed by ETD and BSED detector under ultra-high vacuum by Oxford Instruments (Quanta 250 FEG). It was observed that before electro-annealing surface morphology of the hybrid IAI thin film layer was notably

smooth. Sample thickness of Figure 4.7 is 117.38 nm, Figure 4.8 is 119.26 nm, Figure 4.9 is 123.30 nm.

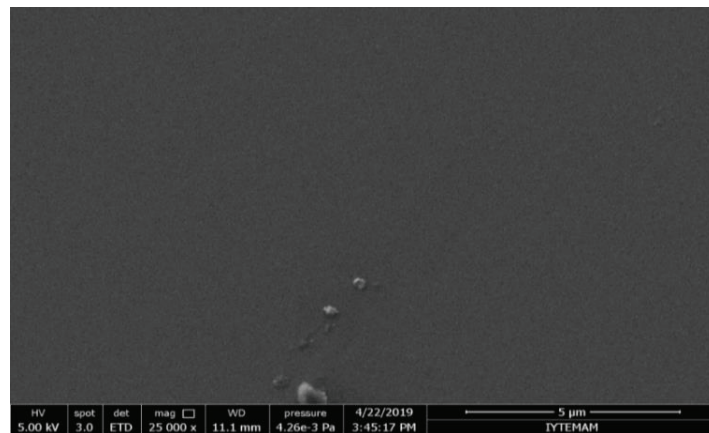


Figure 4.7. SEM image of hybrid 7minITO/17sAg/7minITO thin film.

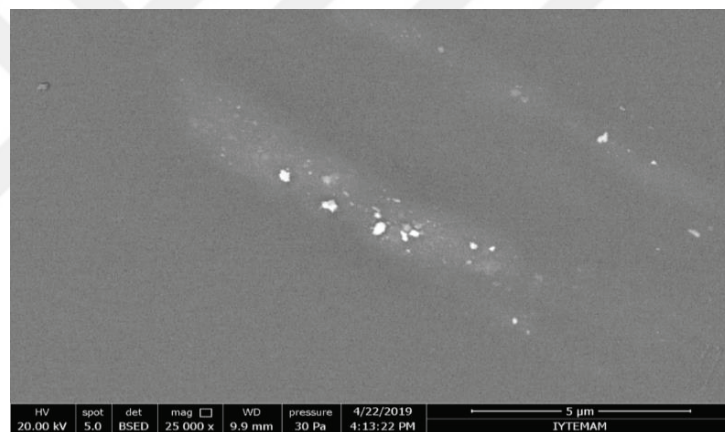


Figure 4.8. SEM image of hybrid 7minITO/19sAg/7min ITO thin film.

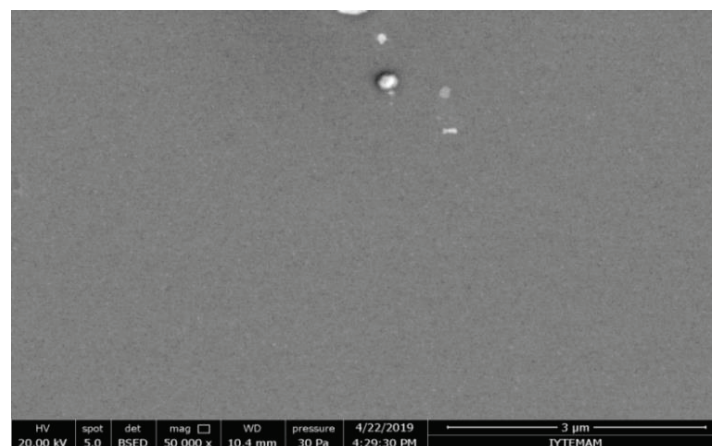


Figure 4.9. SEM image of hybrid 7minITO/21sAg/7 minITO thin film.

4.1.6. Energy Dispersive X-Ray Spectroscopy (EDS) Analysis Result

EDS measurement was performed by BSD detector with HV resolution in 20 kV, 5 spot size under high vacuum in order to determine the elemental composition of hybrid ITO/Ag/ITO electrodes. Table 4.2 shows EDS result of IAI thin film.

Table 4.2. EDS result of hybrid ITO/Ag/ITO thin films on borosilicate glass.

	Element	Wt %	Atomic%
7min-21s-7min	O	54.17	89.41
	Ag	5.43	1.33
	In	36.32	8.35
	Sn	4.08	0.91
7min-19s 7min	O	58.99	91.12
	Ag	5.19	1.19
	In	32.38	6.97
	Sn	3.44	0.72
7min-17s 7min	O	59.22	91.20
	Ag	4.85	1.11
	In	32.50	6.98
	Sn	3.43	0.71

Backscattered electron images show compositional contrast which results from different atomic number elements and their distribution. EDS allows one to identify what those particular elements are and their relative proportions.

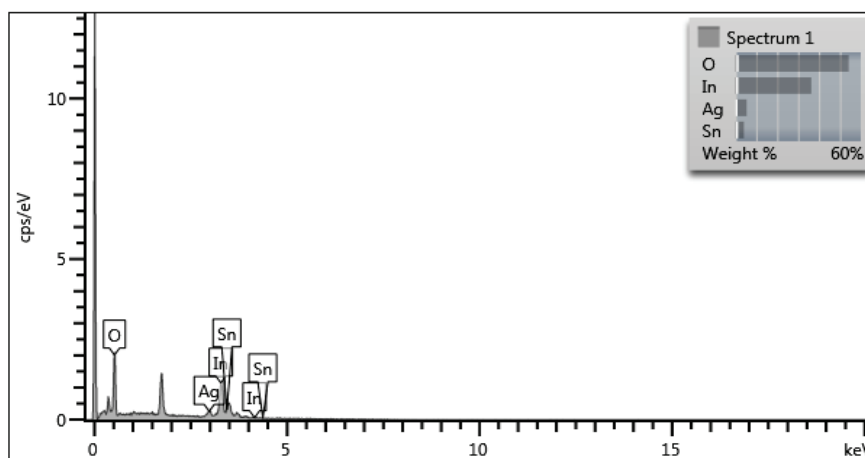


Figure 4.10. EDS graph of 7minITO/21sAg/7minITO layer.

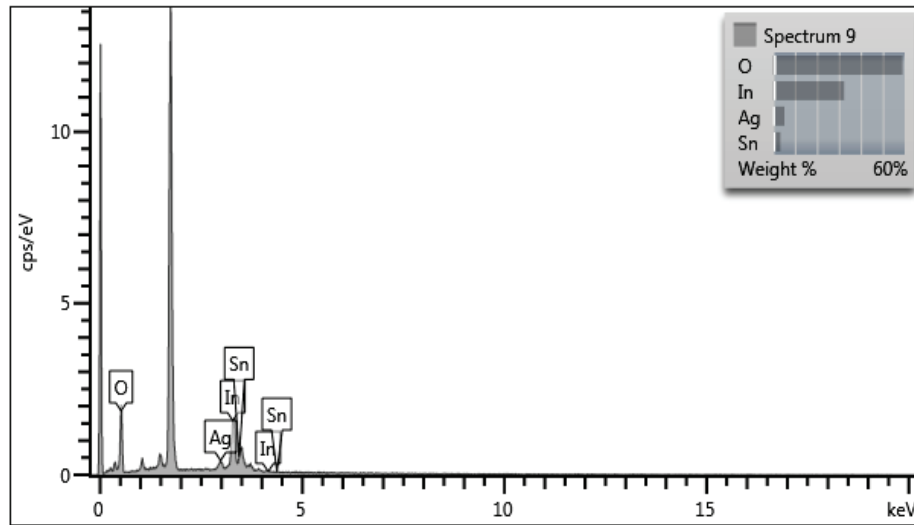


Figure 4.11. EDS graph of 7minITO/19sAg/7minITO layer.

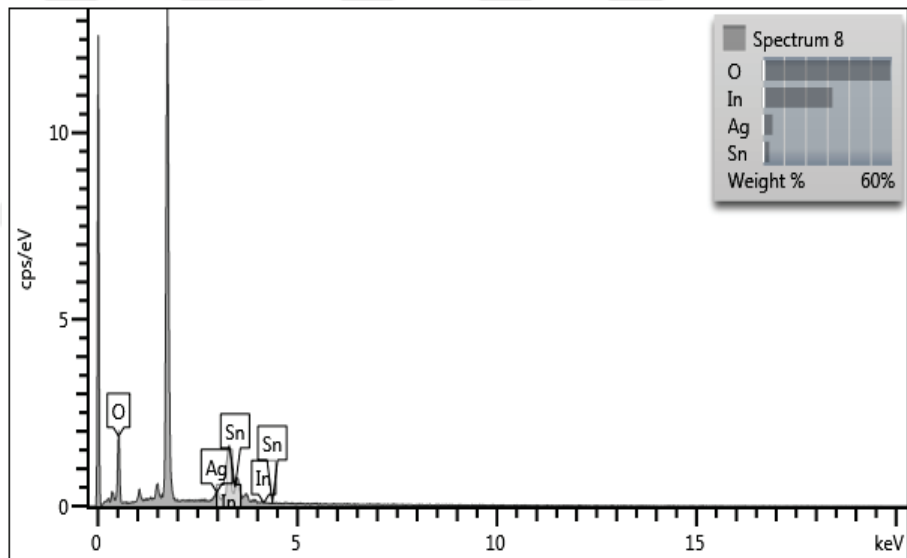


Figure 4.12. EDS graph of 7minITO/17sAg/7minITO layer.

4.1.7. X-Ray Diffraction Analysis Result

Crystallographic information of the hybrid ITO/Ag/ITO electrodes was obtained by XRD analysis. Structural properties of the hybrid IAI layer were characterized by an X-ray diffractometer (XRD) (Philips X'Pert Pro) with $\text{CuK}\alpha$ radiation ($\lambda=0.154$ nm). Figure 4.13. illustrates X-ray diffraction patterns of the hybrid ITO/Ag/ITO layer that deposited at room temperature (RT) and the thickness of the sample shown in Table 4.3.

Analysis performs in the 2θ mode through $10-90^\circ$. Ag has an fcc structure and tendency of it toward 111 orientation in the hybrid system. Peak intensity of metal Ag (111) increased with Ag thickness. For this reason, increasing of Ag layer crystallinity cause the improvement of multilayer's electrical properties. ITO was amorphous as grown hybrid IAI layer.

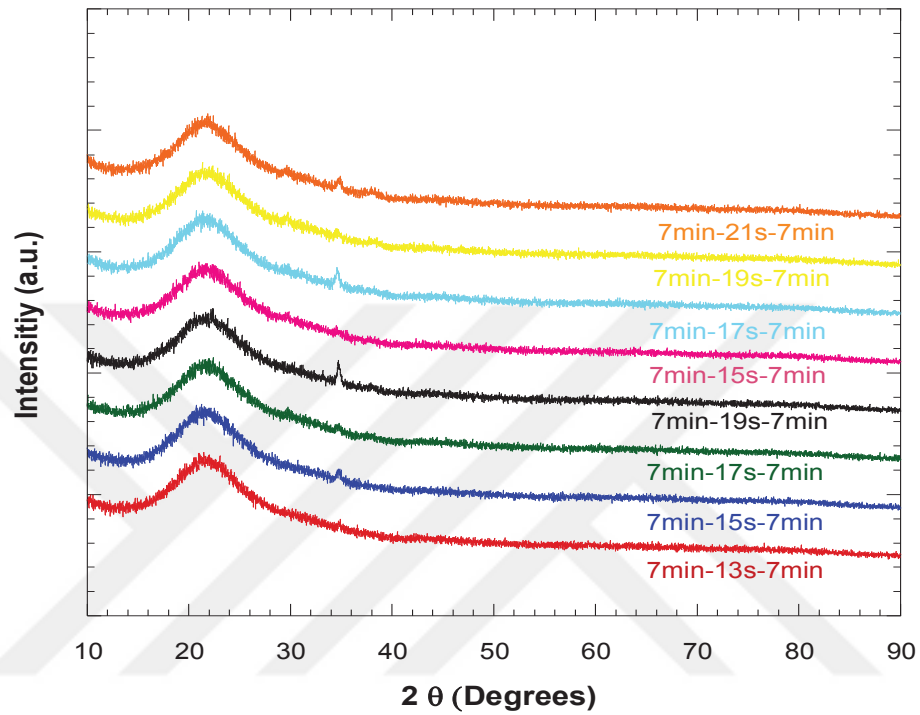


Figure 4.13. XRD patterns of grown samples with different Ag deposition time.

Table 4.3. The thickness of the sample in figure 4.13.

Sample name	Thickness (nm)
7min ITO/13s Ag/7min ITO	113.6
7min ITO/15s Ag/7min ITO	115.4
7min ITO/17s Ag/7min ITO	117.38
7min ITO/19s Ag/7min ITO	119.26
7min ITO/21s Ag/7min ITO	123.30

4.2. Result of Electro-annealed ITO/Ag/ITO Layer

When hybrid ITO/Ag/ITO multiple layers were electro-annealed in air, free oxygen reacts with sample surface which was ITO. As a result of the reaction, the number of ionized oxygen vacancies decreased in the thin film.

Table 4.4. Variation of temperature and current as a function of time.

SET 1									
		ITO- Ag- ITO -1 5.30min-15s-5.30min		ITO- Ag- ITO-2 6min-15s-6min		ITO- Ag- ITO-3 6.30min-15s-6.30min		ITO- Ag- ITO-4 7min-15s-7min	
Time (min)		Temp. (°C)	Current (A)	Temp. (°C)	Current (A)	Temp. (°C)	Current (A)	Temp. (°C)	Current (A)
20V	0	26	3.6			24	4.2	24	4.2
	1	-	-			-	-	-	-
	2	50	3.6					73	4.2
	3	-	-			90	4.8	-	-
	4	-	-			-	-	87	5.4
	5	78	3.6			-	-	-	-
	6	-	-			114	5.4	-	-
	7	-	-			121	6	-	-
	8	-	-			-	6	-	-
	9	-	-			-	6	-	-
	10	92	4.2			132	6	-	-
	11	96	4.2			-	6	121	6
	12	-	-			138	6	-	-
	13	-	-			141	6	-	-
	14	103	4.2			143	6	122	6.6
	15	-	-			148	6	-	-
	16	-	-			-	6	126	6.6
	17	98	4.2			143	6	-	-
	18	-	-			145	6	127	6.6
	19	102	4.2			144	6	-	-
	20	104	4.2			143	6	129	6.6
30V	21	105	6			172	9.6	148	9.6
	22	-	-			-	-	169	9.6
	23	147	7.8			213	9	-	-
	24	-	-			-	-	-	-
	25	-	-			218	9	-	-
	26	173	7.2			-	-	-	-
	27	-	-			222	9	-	-
	28	171	6.6			-	-	212	9
	29	-	-			-	-	-	-
	30	-	-			235	8.4	202	9
	31	172	6.6			228	8.4	-	-
	32	-	-			-	-	-	-
	33	-	-			224	8.4	201	9
	34	167	6.6			222	8.4	202	9
	35	-	-			221	8.4	-	-
	36	172	6.6			-	-	204	9
	37	180	6.6			226	8.4	198	9
	38	170	6.6			-	-	203	9
	39	174	6.6			209	8.4	-	-
	40	174	6.6			207	8.4	202	9
	40V	41	180	9			227	10.2	207
42		207	9			247	10.2	230	11.4
43		222	9			286	9.6	247	11.4
44		232	8.4			283	9.6	261	11.4
45		239	8.4			262	9	268	10.8
46		240	8.4			-	-	260	10.8
47		241	8.4			255	9	261	10.8
48		246	8.4			-	-	263	10.8
49		249	7.8			-	-	260	10.2
50		234	7.8			255	9	264	10.2
51		233	7.8			252	9	250	9.6
52		221	7.8			247	8.4	257	9.6
53		216	7.8			237	8.4	248	9.6
54		214	7.8			231	8.4	257	9.6
55		221	7.8			230	8.4	248	9.6
56		222	7.8			240	8.4	240	9.6
57		230	7.2			234	7.8	236	9
58		202	7.2			222	7.8	228	8.4
59		211	7.8			220	7.8	231	8.4
60		213	7.8			211	7.8	219	8.4

Table 4.5. Variation of temperature and current as a function of time.

		SET 2							
		ITO-Ag-ITO -1 7min-15s-7min		ITO-Ag-ITO-2 7.30min-15s-7.30min		ITO-Ag-ITO-3 8min-15s-8min		ITO-Ag-ITO-4 8.30min-15s-8.30min	
	Time (min)	Temp. (°C)	Current (A)	Temp. (°C)	Current (A)	Temp. (°C)	Current (A)	Temp. (°C)	Current (A)
20V	0	23	7.8	26	5.4	24	4.8	24	5.4
	1	-	7.8	33	5.4	64	4.8	-	-
	2	101	8.4	73	5.4	87	4.8	111	5.4
	3	-	-	85	5.4	103	4.8	133	5.4
	4	122	9	96	5.4	116	5.4	-	-
	5	127	9	101	6	118	5.4	141	6.6
	6	134	9	111	6	133	6	142	7.2
	7	135	9	113	6	137	6	149	7.8
	8	137	8.4	117	6	147	6	154	7.8
	9	145	8.4	119	6	153	7.2	157	7.8
	10	140	8.4	120	6	152	7.2	161	8.4
	11	148	7.8	121	6	150	7.2	170	7.8
	12	150	7.8	124	6	157	7.2	169	8.4
	13	154	7.8	126	6	162	7.2	172	7.8
	14	150	7.8	127	6	159	7.2	169	7.8
	15	154	7.8	128	6	166	7.2	172	7.8
	16	144	7.8	128	6	162	7.2	170	7.8
	17	148	7.2	130	6	164	7.2	171	7.8
	18	150	7.2	128	6	165	7.2	168	7.8
	19	144	7.2	130	6	160	7.2	168	7.8
20	150	7.2	134	6	164	7.2	167	7.8	
30V	21	180	11.4	136	10.2	181	11.4	200	10.8
	22	213	10.8	202	10.2	224	10.8	216	10.8
	23	212	10.8	207	10.2	241	10.2	235	10.2
	24	213	10.8	222	9.6	249	10.2	231	10.2
	25	212	10.8	226	9.6	253	10.2	239	10.2
	26	212	10.8	227	9.6	257	10.2	231	10.2
	27	207	10.8	234	9.6	256	10.2	239	10.2
	28	220	10.2	236	9.6	263	10.2	244	9.6
	29	226	10.8	237	9.6	259	10.2	246	9.6
	30	225	10.2	240	9.6	261	10.2	247	9.6
	31	230	10.2	227	9	257	10.2	243	9.6
	32	225	10.2	226	9.6	259	10.2	240	9.6
	33	214	10.2	227	9.6	259	10.2	242	9.6
	34	211	10.2	228	9	260	10.2	242	9.6
	35	203	10.2	236	9	261	10.2	242	9.6
	36	220	10.2	224	9	258	10.2	239	9.6
	37	228	10.2	223	9	252	10.2	241	9.6
	38	220	10.2	230	9	253	10.2	246	9.6
	39	230	10.2	244	9	257	10.2	251	9.6
	40	234	10.2	232	9	263	10.2	249	9.6
40V	41	239	12.6	261	12	270	12	-	-
	42	272	12	288	11.4	288	10.2	244	9.6
	43	284	12	300	12	281	9.6	242	9
	44	273	11.4	307	10.8	264	10.2	244	8.4
	45	281	10.8	309	10.2	235	9	212	8.4
	46	268	10.8	293	10.8	232	7.2	165	2.4
	47	274	9.6	284	9.6	207	6.6	142	2.4
	48	273	9.6	269	9	207	6.6	131	2.4
	49	274	9	265	8.4	173	6	118	2.4
	50	271	8.4	247	8.4	177	6	108	2.4
	51	267	8.4	234	7.8	166	6	100	2.4
	52	262	7.8	227	7.2	160	5.4	93	2.4
	53	248	7.2	214	7.2	161	5.4	92	2.4
	54	253	7.2	205	6.6	163	5.4	-	-
	55	239	7.2	199	6.6	151	5.4	88	2.4
	56	237	7.2	202	6.6	150	5.4	86	2.4
	57	238	7.2	194	6.6	152	5.4	87	2.4
	58	240	7.2	192	6.6	151	5.4	86	2.4
	59	238	6.6	180	6.6	153	5.4	83	2.4
	60	241	6.6	173	6.6	152	5.4	84	2.4

Table 4.6. Variation of temperature and current as a function of time.

		SET 3							
		ITO- Ag- ITO -1 7min-13s-7min		ITO- Ag- ITO-2 7min-15s-7min		ITO- Ag- ITO-3 7min-17s-7min		ITO- Ag- ITO-4 7min-19s-7min	
	Time (min)	Temp. (°C)	Current (A)	Temp. (°C)	Current (A)	Temp. (°C)	Current (A)	Temp. (°C)	Current (A)
20V	0	24	-	24	-	23	-	28	-
	1	-	-	-	-	-	-	-	-
	2	63	3	-	-	-	-	148	12.6
	3	-	-	78	5.4	-	-	-	-
	4	79	3	116	6.6	250	12.6	-	-
	5	-	-	-	-	-	-	209	13.2
	6	-	-	147	6.6	269	12	-	-
	7	-	-	-	-	-	-	-	-
	8	-	-	151	6.6	-	-	-	-
	9	96	3	-	-	-	-	-	-
	10	94	3	140	7.2	260	12	210	12
	11	-	-	148	6.6	-	-	-	-
	12	-	-	150	6.6	-	-	-	-
	13	-	-	-	-	-	-	224	12
	14	-	-	-	-	-	-	-	-
	15	80	2.4	152	6.6	257	11.4	-	-
	16	-	-	150	6.6	-	-	-	-
	17	73	1.8	150	6.6	-	-	-	-
	18	-	-	-	-	-	-	206	12
	19	-	-	153	6.6	260	11.4	-	-
20	71	1.8	147	6.6	344	15.6	206	12	
30V	21	88	3.6	166	10.2	353	15	281	16.2
	22	-	-	-	-	364	14.4	316	12
	23	-	-	207	9	375	13.8	-	0
	24	99	4.2	-	-	382	14.4	-	-
	25	110	4.8	-	-	380	12	-	-
	26	-	-	236	8.4	-	-	-	-
	27	133	5.4	-	-	322	3	-	-
	28	-	-	-	-	-	-	-	-
	29	144	4.8	-	-	-	-	-	-
	30	149	4.8	-	-	320	1.8	-	-
	31	-	-	-	-	-	0	-	-
	32	152	4.8	211	8.4	-	-	-	-
	33	-	-	-	-	-	-	-	-
	34	-	-	-	-	-	-	-	-
	35	147	4.8	-	-	-	-	-	-
	36	-	-	-	-	-	-	-	-
	37	146	4.8	-	-	-	-	-	-
	38	150	4.8	-	-	-	-	-	-
	39	-	-	-	-	-	-	-	-
	40	140	4.8	216	7.8	-	-	-	-
40V	41	-	-	231	10.2	-	-	-	-
	42	163	5.4	-	-	-	-	-	-
	43	-	-	264	9.6	-	-	-	-
	44	-	-	277	9.6	-	-	-	-
	45	163	5.4	267	9.6	-	-	-	-
	46	-	-	-	0	-	-	-	-
	47	-	-	-	-	-	-	-	-
	48	153	4.2	-	-	-	-	-	-
	49	-	-	-	-	-	-	-	-
	50	154	4.8	-	-	-	-	-	-
	51	-	-	-	-	-	-	-	-
	52	-	-	-	-	-	-	-	-
	53	-	-	-	-	-	-	-	-
	54	-	-	-	-	-	-	-	-
	55	-	-	-	-	-	-	-	-
	56	-	-	-	-	-	-	-	-
	57	-	-	-	-	-	-	-	-
	58	146	4.2	-	-	-	-	-	-
	59	-	-	-	-	-	-	-	-
	60	148	4.2	-	-	-	-	-	-

Table 4.7. Variation of temperature and current as a function of time.

		SET 4							
		ITO- Ag- ITO -1 7min-15s-7min		ITO- Ag- ITO-2 7min-17s-7min		ITO- Ag- ITO-3 7min-19s-7min		ITO- Ag- ITO-4 7min-21s-7min	
Time (min)	Temp. (°C)	Current (A)	Temp. (°C)	Current (A)	Temp. (°C)	Current (A)	Temp. (°C)	Current (A)	
20V	0	24	-	28	-	26	-	23	-
	1	84	9	73	9	-	-	-	-
	2	136	9.6	143	10.2	-	-	184	15.6
	3	-	-	-	-	-	-	-	-
	4	-	-	-	-	-	-	-	-
	5	170	9.6	172	10.2	225	14.4	247	14.4
	6	-	-	180	10.2	246	13.8	-	-
	7	164	8.4	-	-	238	13.8	-	-
	8	-	-	181	9.6	-	-	232	13.8
	9	-	-	187	9.6	254	13.8	-	-
	10	156	8.4	191	9.6	254	13.8	243	13.8
	11	-	-	-	-	-	-	-	-
	12	-	-	180	9.6	-	-	-	-
	13	-	-	-	-	-	-	233	13.2
	14	160	7.8	186	9.6	-	-	224	13.2
	15	157	7.8	191	9.6	240	13.2	220	13.2
	16	-	-	184	9.6	-	-	283	15
	17	149	7.8	192	9.6	244	13.2	292	14.4
	18	156	7.8	192	9.6	-	-	-	-
	19	147	7.2	-	-	238	13.2	-	-
	20	147	7.2	189	9.6	230	13.2	276	15
21	167	9.6	245	14.4	301	16.8	311	16.2	
30V	22	159	6.6	278	14.4	328	15.6	-	-
	23	-	-	298	13.8	-	-	212	15
	24	-	-	-	-	321	15	-	-
	25	156	6.6	309	13.8	322	15	248	9.6
	26	-	-	-	-	-	-	243	8.4
	27	145	6.6	287	13.2	316	14.4	-	-
	28	-	-	291	12.6	-	-	-	-
	29	-	-	291	12.6	274	7.2	-	-
	30	139	6	292	12.6	224	6	217	8.4
	31	-	-	290	12.6	-	-	-	0
	32	-	-	292	12.6	161	4.8	-	-
	33	-	-	300	12.6	152	4.2	-	-
	34	-	-	287	12	149	4.2	-	-
	35	140	6	280	12	-	-	-	-
	36	-	-	288	12	-	-	-	-
	37	133	6	292	12	132	4.2	-	-
	38	-	-	271	12	133	4.2	-	-
	39	-	-	271	12	-	-	-	-
	40	136	6.6	-	-	128	4.2	-	-
	40V	41	136	6.6	-	-	-	-	-
42		150	5.4	-	-	132	3	-	-
43		-	-	257	4.2	-	-	-	-
44		150	4.2	227	4.2	-	-	-	-
45		147	3.6	229	4.2	114	3	-	-
46		-	-	240	4.2	-	-	-	-
47		-	-	224	4.2	112	3	-	-
48		120	3	221	4.2	-	-	-	-
49		-	-	-	-	111	3	-	-
50		128	3	226	4.2	110	3	-	-
51		117	3	230	4.2	-	0	-	-
52		-	-	223	4.2	-	-	-	-
53		113	3	231	4.2	-	-	-	-
54		-	-	215	4.2	-	-	-	-
55		112	3	222	4.2	-	-	-	-
56		109	3	218	4.2	-	-	-	-
57		-	-	218	4.2	-	-	-	-
58		-	-	235	-	-	-	-	-
59		108	2.4	247	-	-	-	-	-
60		107	2.4	247	-	-	-	-	-

The temperature of the film increases oxygen vacancies decrease highly and impurity scattering becomes weaker and so crystal grain was grown. Result of further grain boundary cause to more crystallinity. Grain boundary provides free carrier electrons in film and hence carrier concentration increases after the electro-annealing. Optical transmission data clearly indicated electro-annealing in air enhanced the IAI multilayer in terms of their optoelectrical aspects. Four point probe method analysis is also supported transmission result. The highest transmission value after the electro-annealing was obtained for 7min-15s-7min deposited sample. The resistance of the hybrid IAI layer decreased as the substrate temperature increases. When the thickness of ITO was increased with fixed Ag thickness, the resistance was decreased. Because this may be an increment in the number of carrier concentration grain size and crystallization. Thickness increasing of metal Ag between ITO film caused to the decreasing of sheet resistance of the IAI film. The best sheet resistivity was obtained from sample 7min-21s-7min at 292 °C. The applied voltage was 20 AC Volt and its current value was 14.40 A. Sputtering time parameters and layer properties of film shown in Table 4.8.

Comparison between sheet resistance of IAI samples before electro-annealing and after electro annealing is shown in Figure 4.14.

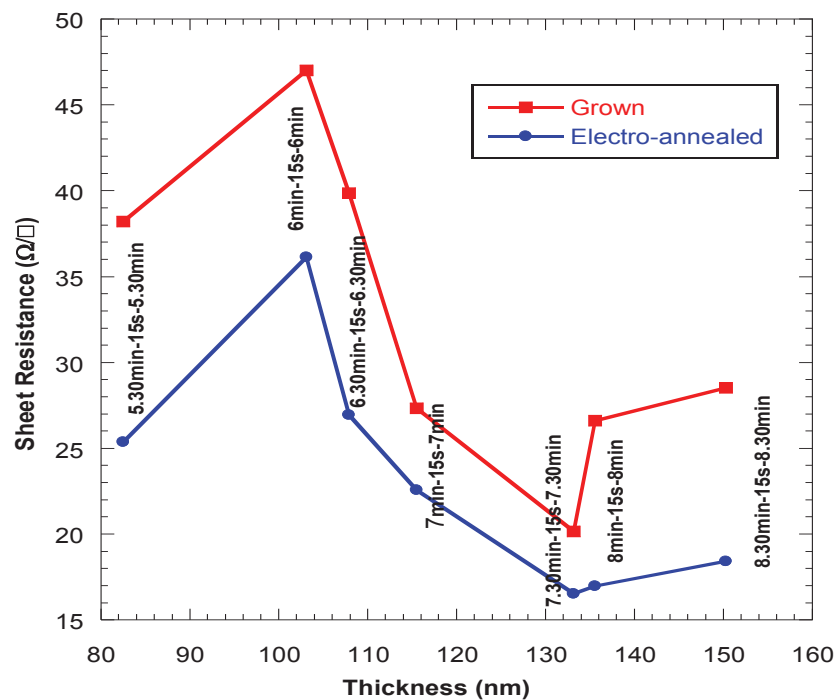


Figure 4.14: Improvement of sheet resistance after electro-annealing.

Table 4.8. Sputtering time parameters and layer properties of IAI film both before and after electro annealing.

	Sputtering Time			(T%) 550nm	(T%) after electro- annealed	R_s (Ω/\square)	R_s (Ω/\square) after electro- annealed	Thickness (nm)
	ITO min	Ag s	ITO min					
SET 1	5.30	15	5.30	71.920	79.260	38.19	25.36	82.5
	6	15	6	67.740	78.500	47.00	36.14	103.1
	6.30	15	6.30	75.430	81.430	39.86	26.94	107.9
	7	15	7	81.350	82.450	27.32	22.55	115.5
SET 2	7	15	7	85.490	88.010	19.24	23.43	117.4
	7.30	15	7.30	84.260	87.660	20.15	16.53	133.2
	8	15	8	76.380	83.780	26.59	16.98	135.6
	8.30	15	8.30	75.430	86.950	28.53	18.41	150.3
SET 3	7	13	7	76.520	79.370	38.95	24.98	113.62
	7	15	7	78.850	80.160	25.25	20.20	115.4
	7	17	7	82.740	85.920	16.39	13.58	117.38
	7	19	7	82.750	86.080	11.99	11.62	119.26
SET 4	7	15	7	88.260	88.870	16.87	15.62	116.3
	7	17	7	88.730	86.800	13.58	13.92	118.1
	7	19	7	87.810	88.030	11.54	10.52	119.26
	7	21	7	86.930	87.460	9.05	8.71	123.30

4.2.1. Transmission of ITO/Ag/ITO layer after electro-annealing

The electro-annealing is applied according to Figure 3.8. Electro-annealing shows better transmission compare with grown sample.

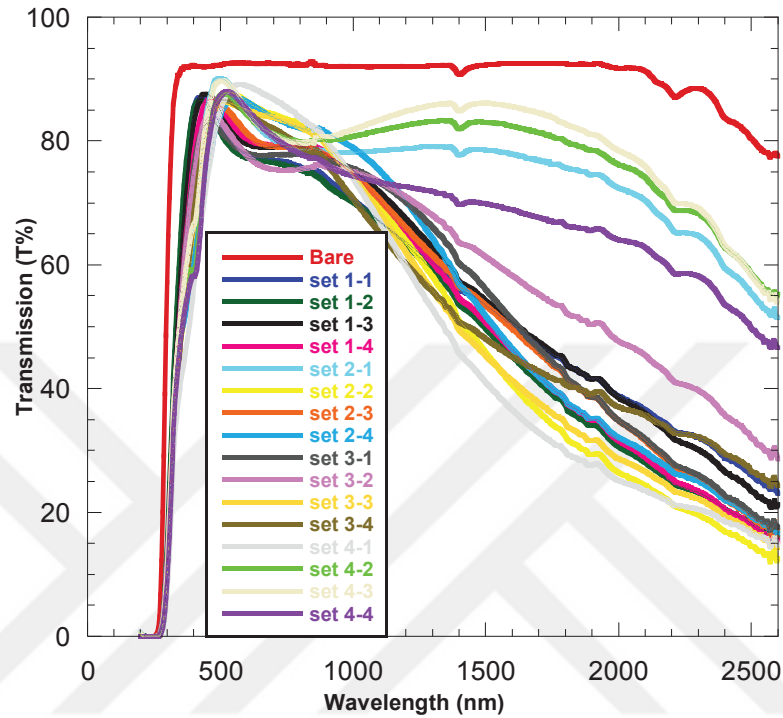


Figure 4.15. Effect of electro-annealing on transmission value of different samples.

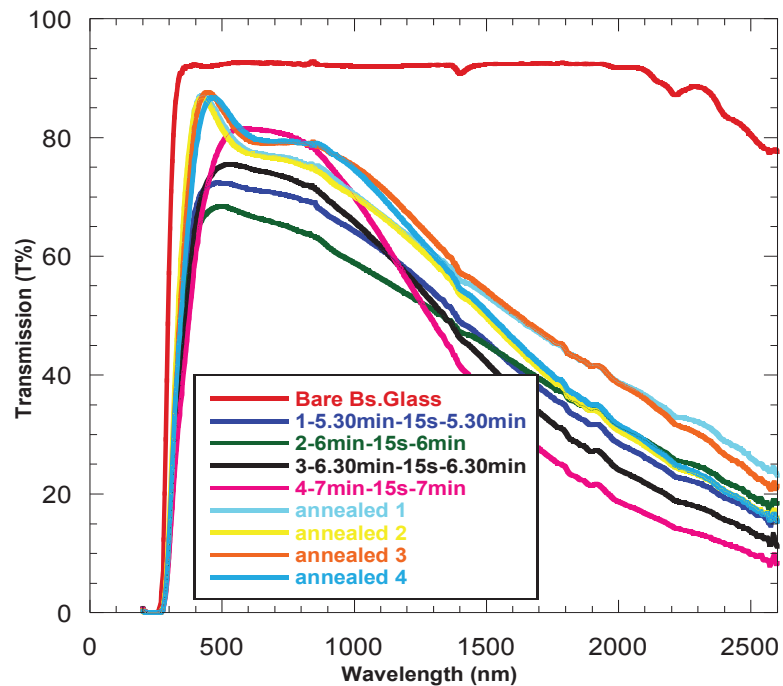


Figure 4.16. Transmission spectra of grown and electro-annealed samples.

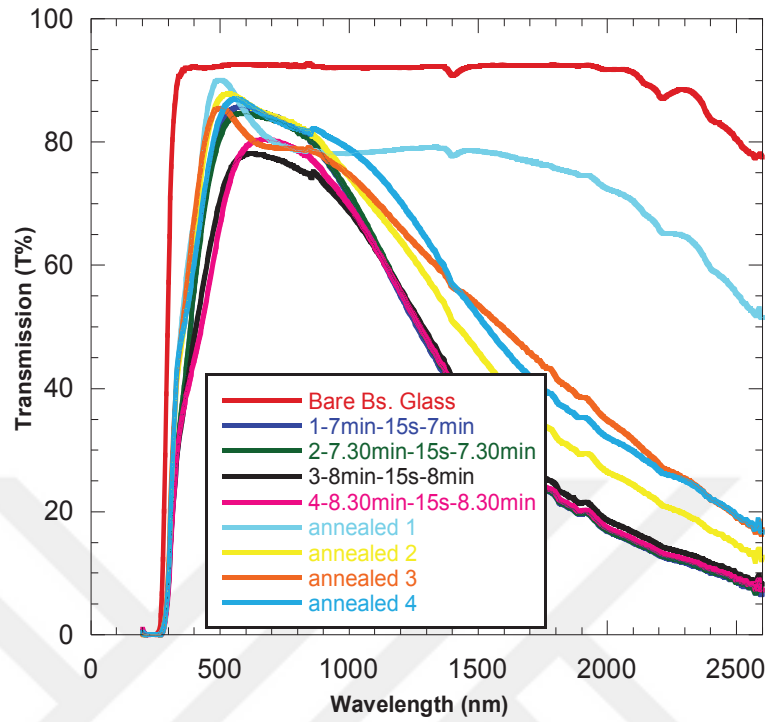


Figure 4.17. Transmission spectra of grown and electro-annealed samples.

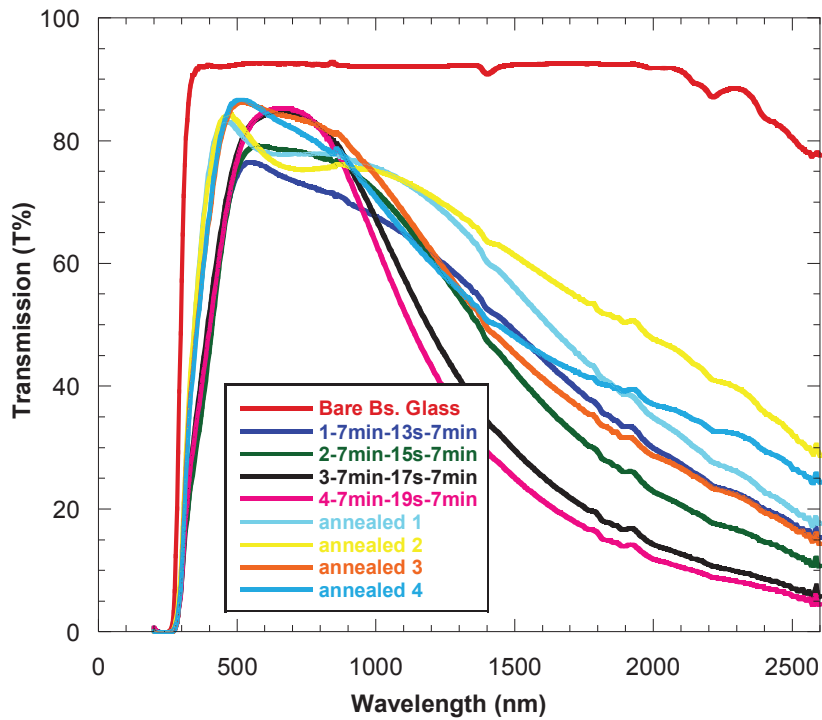


Figure 4.18. Transmission spectra of grown and electro-annealed samples.

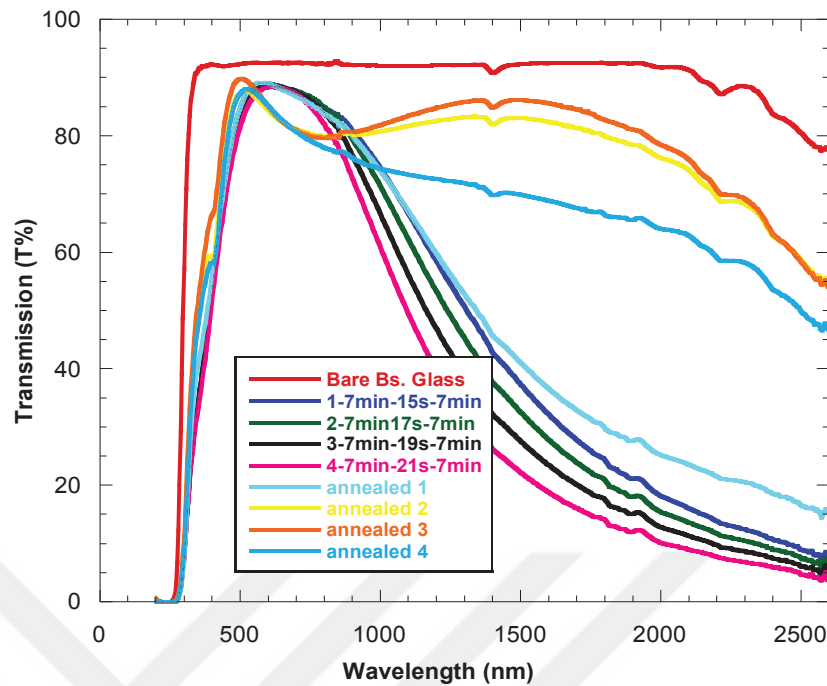


Figure 4.19. Transmission spectra of grown and electro-annealed samples.

4.2.2. Band Gap Energy of Grown and Electro-annealed Samples

In this subsection in order to estimate the bandgap energy of the hybrid IAI layer absorption coefficient versus photon energy graph of films was used. Following Figure 4.20 shows the varies in absorption coefficient (α^2) with respect to photon energy ($h\nu$) for different top and bottom ITO thicknesses. Silver thickness was constant in all hybrid IAI layers and deposited 15 seconds. The silver thickness value is 12.4 nm. While the thickness of the hybrid IAI thin films was increased, the resistance of film was decreased. Result of this decreased, the bandgap of the film is increased. Bandgap widening of hybrid IAI thin films is expected to happen due to higher carrier concentration and also based on Burstein-Moss shift band gap widening can be explained. Electron-electron and also electron-impurity scattering is caused to bandgap narrowing at high carrier concentration.

The optical band gap of ITO is 3.8 eV. In Figure 4.20, the calculated bandgap was 3.8 eV for ITO. Bandgap energy of hybrid IAI films orange shifts with an increased due to adding metal silver. The increasing carrier concentration of IAI film with the inclusion of embedded Ag layer can be figured out based on Schottky theory. Electron

transfer from Ag to ITO is occurred to align the Fermi levels due to the smaller work function of Ag from ITO (Srivastava, 2007). Accumulation type contact form occurs and there is band bending at the contact (Kim et al., 2004).

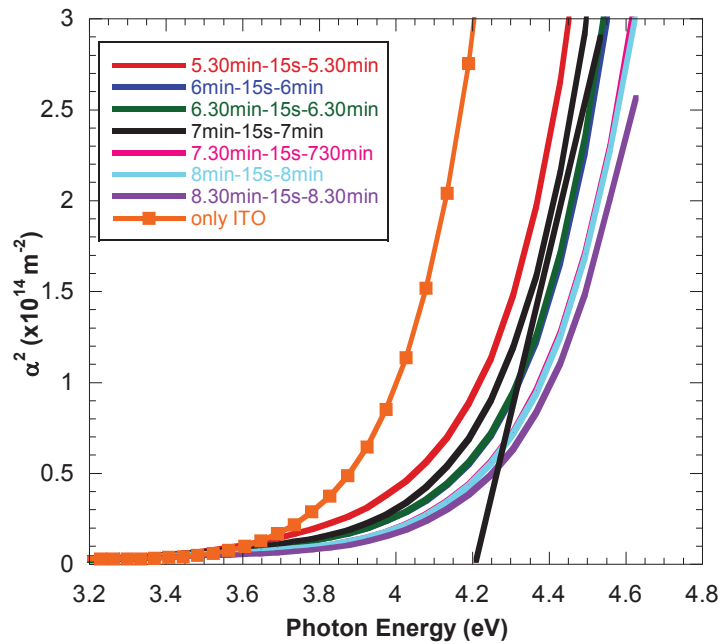


Figure 4.20. Graph of absorption coefficient (α^2) versus photon energy (eV) for grown hybrid IAI films with different ITO same Ag thicknesses.

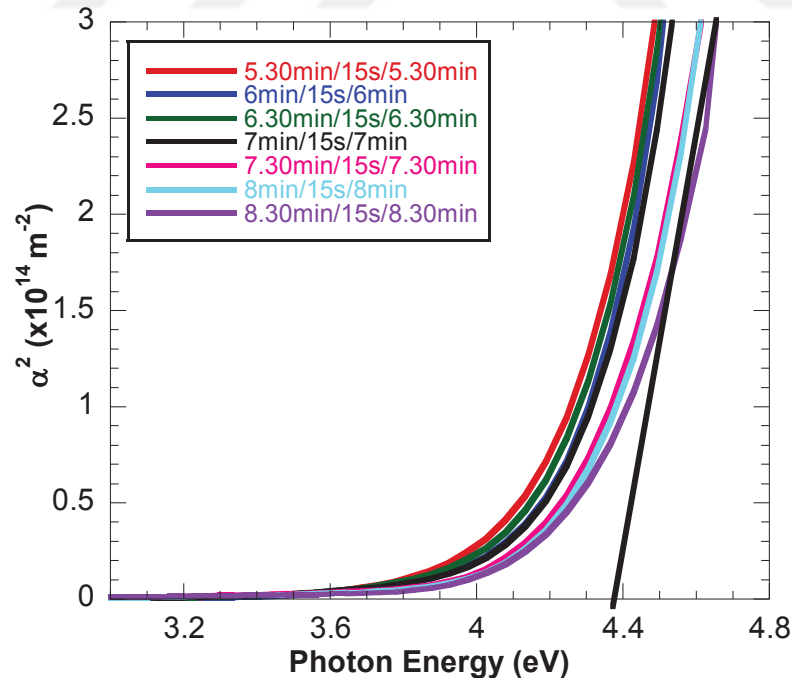


Figure 4.21. Graph of absorption coefficient (α^2) versus photon energy (eV) for the electro-annealed hybrid IAI films with different ITO same Ag thicknesses.

Figure 4.21 shows the changes in absorption coefficient α^2 with respect to the incident beam energies (photon energy, the) measured for hybrid IAI layers grown on borosilicate glass after the electro-annealing. The relation between the absorption coefficient and energy gap was calculated using the following Formula 4.2,

$$\alpha(h\nu)=A[h\nu-E_g]^{(1/2)} \quad (4.2)$$

Absorption values were calculated using the following Equation 4.3,

$$T-R=e^{-\alpha t} \quad (4.3)$$

where R is the transmittance and T is the reflectance and small t is the thickness of the hybrid IAI film. R was neglected because its value is very low. Therefore, the absorption coefficient was reduced to the following Equation 4.4,

$$\alpha^2 = \frac{(\ln T)^2}{t^2} \quad (4.4)$$

Direct optical band gap value of the as-grown hybrid IAI films is smaller than the electro-annealed films. This is due to the high carrier concentration. The carrier concentration of the hybrid IAI layers increases with an electrical current which filling the energy levels in the bottom conduction band. While resistivity of films decreased, the bandgap of hybrid IAI film was increased with respect to the increased annealing current.

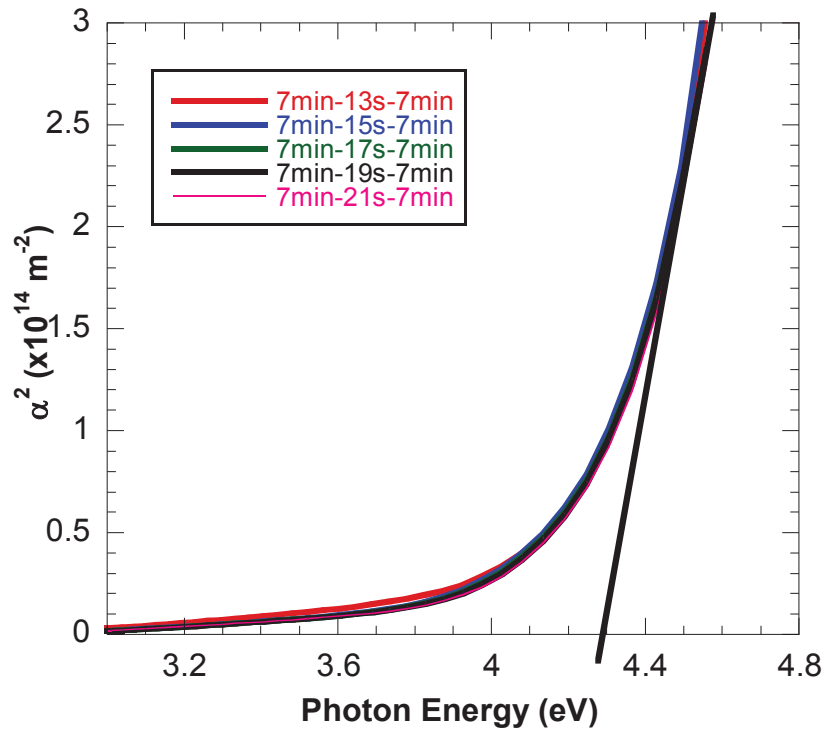


Figure 4.22. Graph of absorption coefficient (α^2) versus photon energy (eV) for the grown hybrid IAI films with the same ITO different Ag thicknesses.

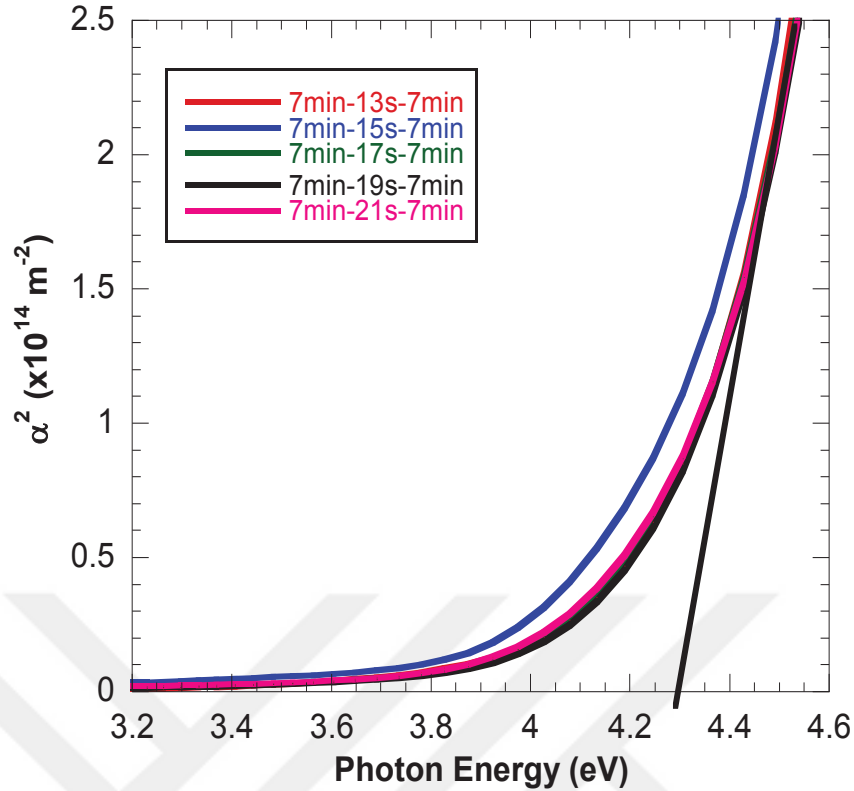


Figure 4.23. Graph of absorption coefficient (α^2) versus photon energy (eV) for the electro-annealed hybrid IAI films with the same ITO different Ag thicknesses.

4.2.3. SEM Images of ITO/Ag/ITO Layer After Electro-annealing

Effect of electro-annealing on surface morphologies of hybrid 7min/15s/7min thin film can be seen in Figure 4.24. In this image, Ag interlayer was deposited 15 seconds between two ITO. The image in Figure 4.25 was taken secondary electron detector under ultra-high resolution. After growth hybrid IAI layers electro-annealing treatment was performed to improve structural, optical and electrical characteristics. Crystallization was increased with annealing. Before the electro-annealing process, surface the morphology of IAI film was smooth. Silver islands are distributed randomly on the surface of ITO that cause to degradation of optoelectronic performance of the electrode. By increasing the thickness of the Ag layer, the Ag islands have started to bind to each other and have formed a continuous film. After electro-annealing process scanning electron microscope analysis confirmed that crystal grain was grown and becomes more clear. Diameter and shape of grain are varied under different conditions that are relative to substrate and growth temperature. Electro-annealing was one of the

fundamental driving force in order to form clear and bigger grain. The ability of the upper ITO layer resist the humidity penetration was also vital to the durability of the hybrid IAI thin film (Chen et al., 2007).

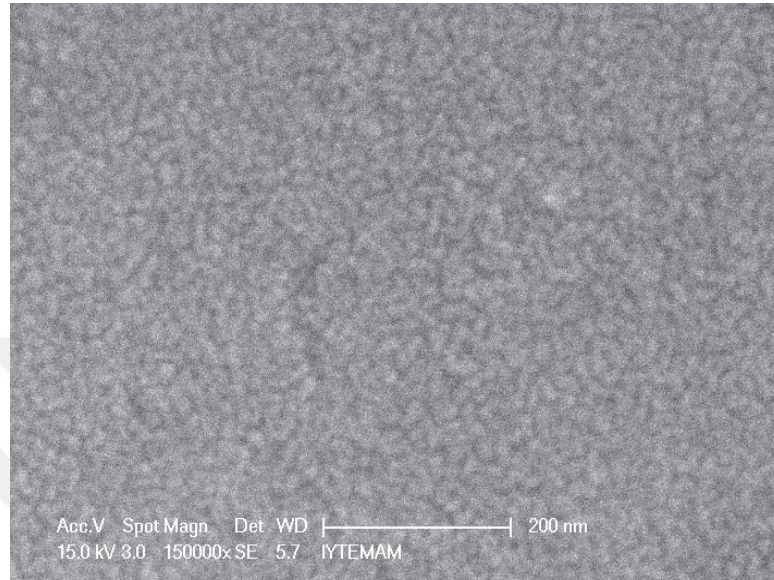


Figure 4.24. Sem image of 7minITO/15sAg/7minITO film after the electro-annealing.

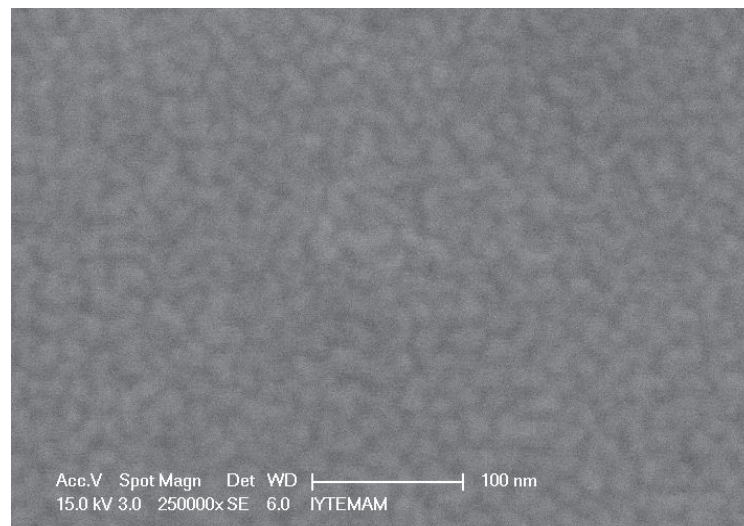


Figure 4.25. Sem image of 7minITO/17sAg/7min ITO film after the electro-annealing.

4.2.4. X-Ray Diffraction Analysis Result After Electro-annealing

Figure 4.26 shows XRD patterns of electro-annealed hybrid IAI films which annealed in air. The applied voltage was increased to 20, 30, 40 AC Volts respectively. The increasing electro-annealing current has improved the crystallinity of hybrid IAI thin films. When the temperature was increased, the intensity of the peaks increases. During annealing, the material tends to lose the extra strain energy and revert to the original condition. This is achieved by the processes of recovery.

In Figure 4.27 and Figure 4.28 shows XRD pattern comparison between before and after electro-annealed sample.

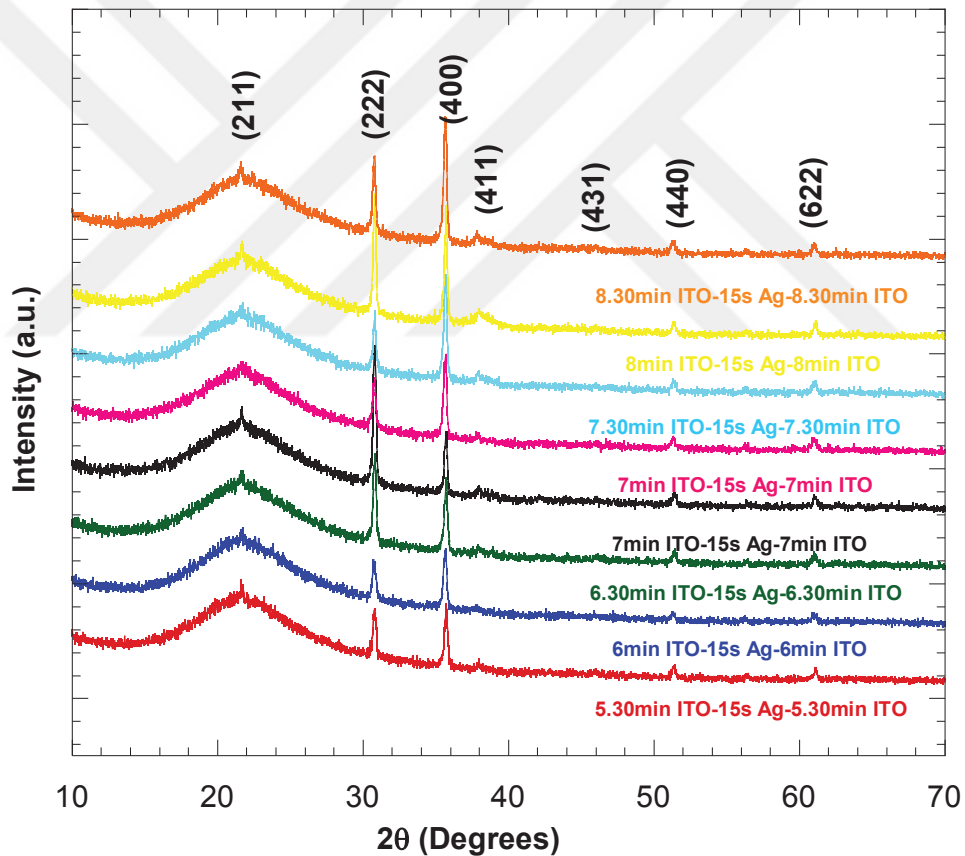


Figure 4.26. XRD patterns of electro-annealed hybrid IAI thin films.

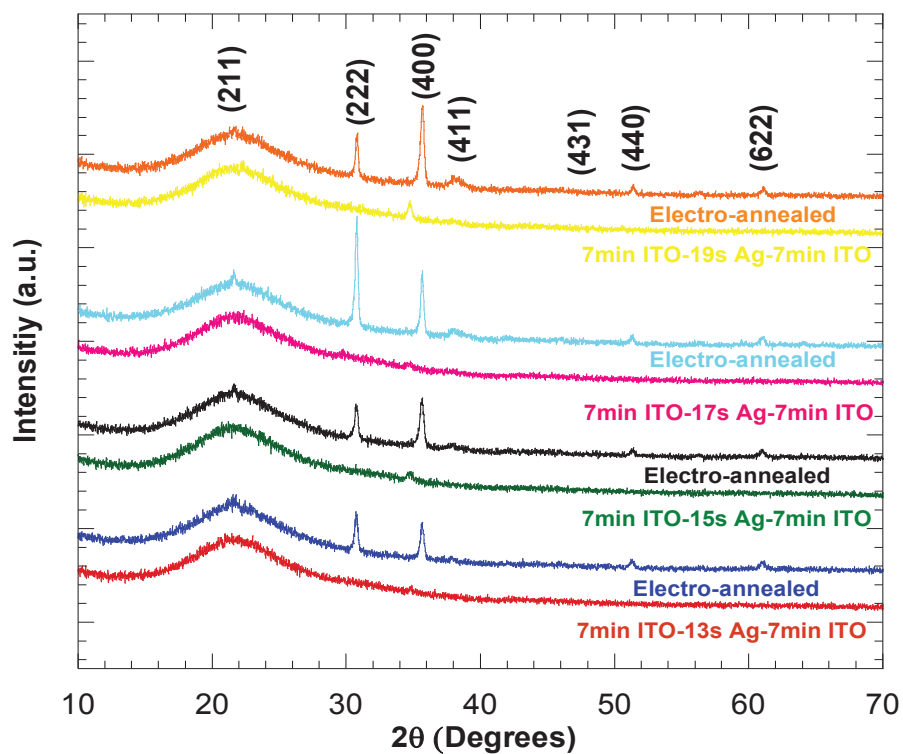


Figure 4.27. XRD pattern of samples after the electro-annealing.

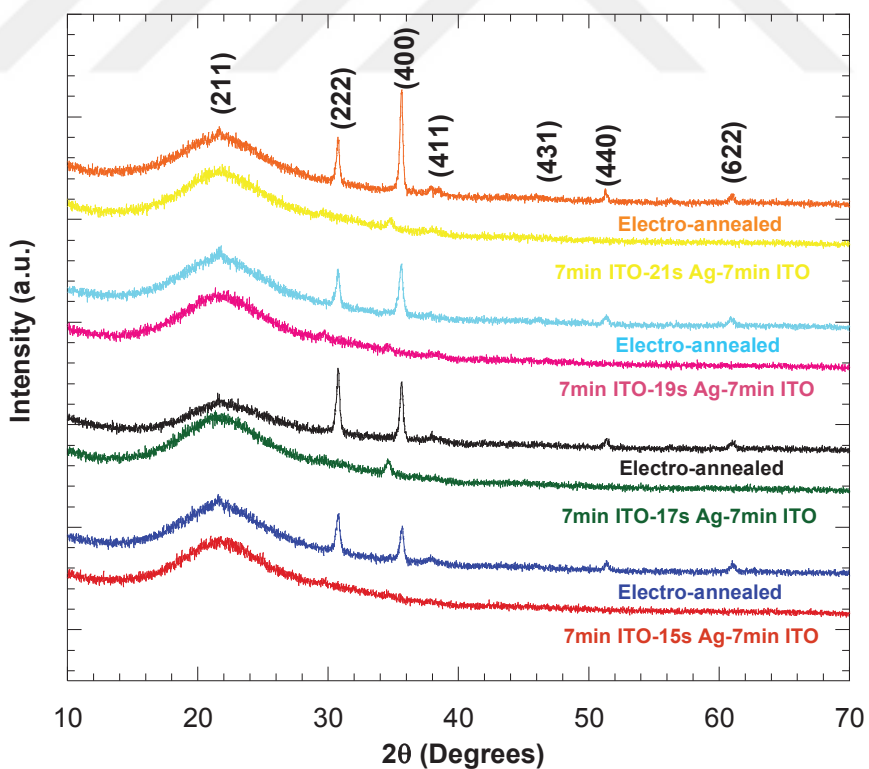


Figure 4.28. XRD pattern of samples after the electro-annealing.

4.2.5. Variation of Temperature and Time

Increase in the average grain size on further annealing after all the cold-worked material was recrystallized. A larger grain will reduce the strength and the toughness of the material.

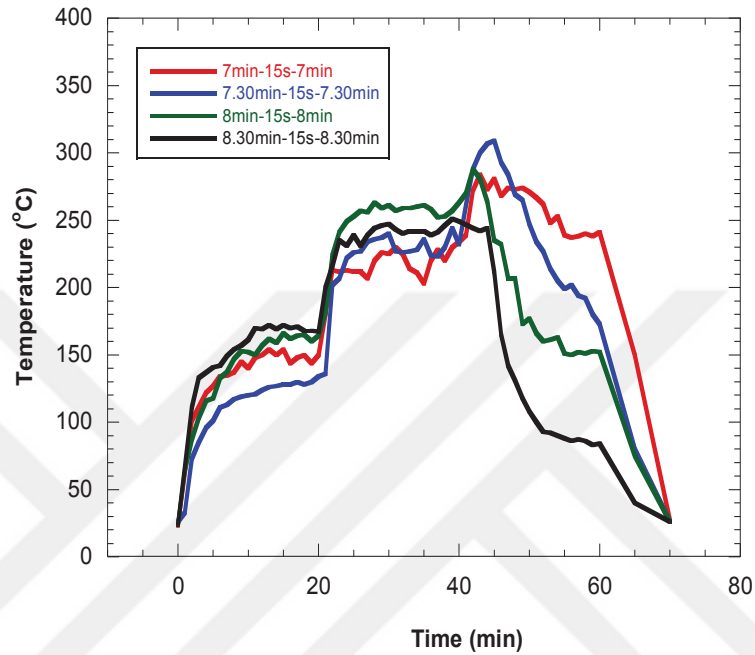


Figure 4.29. Change of temperature versus time electro-annealed hybrid IAI films with different ITO thicknesses.

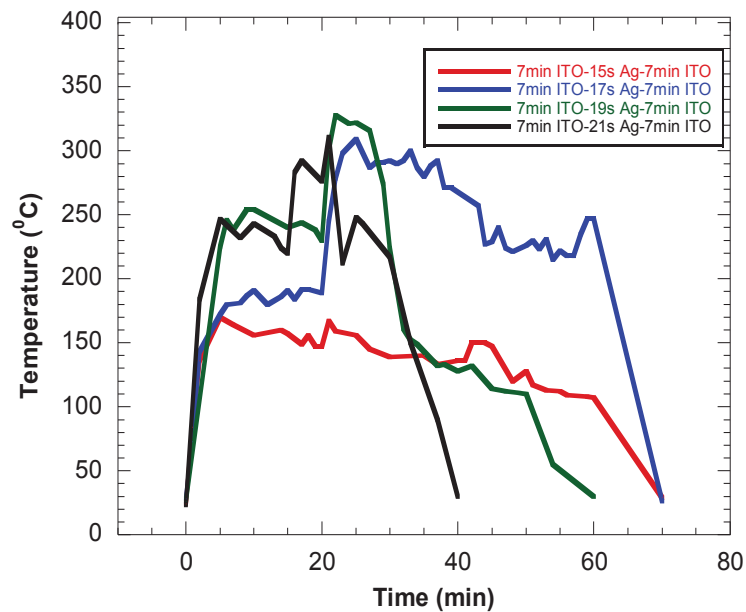


Figure 4.30. Change of temperature versus time electro-annealed hybrid IAI films with different Ag thicknesses.

CHAPTER 5

CONCLUSION

This thesis has consisted of three main contributions. Initially, it has conducted an experimental investigation of depositing hybrid IAI thin film on borosilicate glass. It was intended that IAI multilayer films properties would provide useful for optoelectronic devices for use in different implementations. Parametric study of the hybrid IAI films thicknesses was done. In the second part electro-annealing applied to deposited hybrid IAI films. Finally, in the last part, the samples were going to be compared between the electro-annealed IAI films and the hybrid IAI layer structure, which was not electro-annealing.

In part one of this thesis, hybrid IAI film thicknesses from 80 to 124 nm were deposited by using dc magnetron sputtering onto borosilicate substrate and analyzed with XRD and SEM. First, ITO deposited time was changed from 5.30min. to 8.30min. and silver deposited time was kept constant at 15 seconds. The results indicate that the best sheet resistivity with $19.24 \Omega/\square$ were achieved at sample 7min ITO/15sAg/7min ITO. Its transmittance value was 85.49%. Secondly, ITO deposited time fixed at 7 min. and silver deposited time changed 13, 15, 17, 19, 21 seconds, respectively. While silver thickness was increased, the sheet resistance of hybrid IAI thin film was decreased. The best resistance was obtained $9.05 \Omega/\square$ for 21 second sputtering Ag. However, 7min ITO/21sAg/7min ITO films showed lower transmittance because of the increased light absorption in the Ag layer. Maximum transmittance value was achieved at 88.260%. While the thickness of the hybrid IAI thin films was increased, the resistivity of film was decreased. Result of this decreased, the bandgap of the film was increased. Bandgap widening of hybrid IAI thin films was expected to happen due to higher carrier concentration and also based on Burstein-Moss shift band gap widening can be explained. XRD results indicate that the hybrid IAI electrode without electro annealing was amorphous. SEM result was shown that before electro-annealing surface morphology of the hybrid film was notably smooth. The essential achievement of this thesis improved the conductivity and overall transmittance of the hybrid IAI films. For this reason, electro-annealing was applied to all deposited sample in air. Effect of electrical current was investigated and the result shows that while the thickness of ITO in the hybrid layer was increased, applied electric current increased

leads to decreasing R_s of the hybrid films. Increasing the interaction of oxygen atoms with indium was provided by the lower temperature of the hybrid IAI film. Decreasing of R_s and intensification of the oxygen vacancy concentration give rise to $\text{In}_2\text{O}_{3-x}$ phase was formed. High-temperature cause to the interaction of the residual oxygen atoms with indium atoms and with $\text{In}_2\text{O}_{3-x}$ phase both inside and top surface. Subsequently, In_2O_3 phase was formed. The formation of In_2O_3 has reduced the oxygen vacancy concentration and increased the R_s . The maximum transmission which was 88.87% observed in sample 7min ITO/15sAg/7min ITO and sheet resistance decreased with increasing mid-layer metal Ag thicknesses. Sheet resistance was observed in sample 7min ITO/21sAg/7min ITO and its value were $8.71 \Omega/\square$. After the electro-annealing XRD result showed that increasing Ag thickness from 13 second to 21 second, the crystallinity of hybrid IAI thin films was improved and sheet resistance of hybrid IAI layers depend upon the (400 plane) due to the accommodates the oxygen vacancies on its plane. SEM results showed that crystal grain was grown and becomes more cleared by applying electrical current passing through the Ag layer in the hybrid IAI films.

This thesis has improved the understanding of the electrical current effect on multilayer IAI films structure and the performance of the electrode. Undoubtedly, in the future, the hybrid electrode technology will be benefited from plenty of technology. Thus, there is an oodles of room to work these hybrid films with electro-annealing and it would surely benefit us for many purposes.

REFERENCES

- Akkad, F. E., S. Joseph. (2012). Physicochemical Characterization of Point Defects in Fluorine Doped Tin Oxide Films. *Journal of Applied Physics*. 112 (2): 023501.
- Barber, Z. H. (2005). The Control of Thin Film Deposition and Recent Developments in Oxide Film Growth. *Journal of Materials Chemistry*. 16, 334-344
- Bartella, J., J. Schroeder, and K. Witting. (2001). Characterization of ITO and TiO_xN_y Films by Spectroscopic Ellipsometry. *Applied Surface Science*. 179 (1-4): 181-90.
- Brown, A. R., D. D. C Bradley, J. H. Burroughs, R. H. Friend, N. C. Greenham, P. L. Burn, A. B. Holmes and A Kraft. (1992). Mechanism of Enhanced Quantum Efficiency in Light-Emitting Diode Based on a Poly(p-Phenylenevinylene) Derivative. *Applied Physics Letters*. 61: 3183.
- Chen, S.W., C.Y. Bai, C. C. Jain, C. J. Zhan, and C. H. Koo. (2007). Durability of Indium Tin Oxide-Silver-Indium Tin Oxide Films against Moisture Investigated Through The Wettability of The Top Oxide Layer. 48, 8: 2230-2234
- Cheng, C. H., and J. M. Ting. (2007). Transparent Conducting GZO, Pt/GZO, and GZO/Pt/GZO Thin Films. *Thin Solid Films* 516 (2-4): 203-7.
- Cheong, H.G., J.H. Kim, J. H. Song, U. Jeong, and J. W. Park. (2015). Highly Flexible Transparent Thin Film Heaters Based on Silver Nanowires and Aluminum Zinc Oxides. *Thin Solid Films*. 589: 633-41.
- Chiang, C. K., C. R. Fincher, Y. W. Park, A. J. Heeger, H. Shirakawa, E. J. Louis, S. C. Gau, and Alan G. MacDiarmid. 1977. Electrical Conductivity in Doped Polyacetylene. *Physical Review Letters*. 39 (17): 1098-1101.
- Danielzik, B., M. Heming, D. Krause and A. Thelen. (2003). *Thin Films on Glass: An Established Technology*. 1-21.
- Demirhan Y., H. Koseoglu, F. Turkoglu, Z. Uyanik, G. Aygun, L. Ozyuzer. (2019). The Controllable Deposition of Large Area Roll-to-Roll Sputtered Ito Thin Films for Photovoltaic Applications. *Renewable Energy*. 1549-1559.
- Dweydari, A. W., and C. H. B. Mee. (1973). Oxygen Adsorption on the (111) Face of Silver. *Physica Status Solid. (A)* 17 (1): 247-50.

- Ederth, J. (2003). Electrical Transport in Nanoparticle Thin Films of Gold and Indium Tin Oxide. *Acta Universitatis Upsaliensis. Comprehensive Summaries of Uppsala Dissertations from the Faculty of Science and Technology* 790.
- Exarhos, G. J. and X. D. Zhou. (2007). Discovery-Based Design of Transparent Conducting Oxide Films. *Thin Solid Films* 515 (18): 7025–52.
- Farnsworth, H. E., and R. P. Winch. (1940). Photoelectric Work Functions of (100) and (111) Faces of Silver Single Crystals and Their Contact Potential Difference. *Physical Review* 58 (9): 812–19.
- Fortunato, E., L. Raniero, L. Silva, A. Goncalves, A. Pimental, P Barquinha, L Pereira, G. Goncalves, and I. Ferreira. (2008). Highly Stable Transparent and Conducting Gallium-Doped Zinc Oxide Thin Films for Photovoltaic Applications. *Solar Energy Materials and Solar Cells*. 92 (12): 1605–10.
- Geoffroy, C., G. Campet, F. Menil, J. Portier, J. Salardenne and G. Couturier. (1991). Optical and Electrical Properties of SnO₂:F Thin Films Obtained by R.F. Sputtering With Various Targets. *Active and Passive Electronic Components*. 14 (3): 111–18.
- Hong, C. H, Y. J. Jo, H. A. Kim, M. J. Park and J. S. Kwak. (2012). Improved Electrical and Optical Properties of ITO/Ag/ITO Films by Using Electron Beam Irradiation and Their Application to Ultraviolet Light Emitting Diode as Highly Transparent p-Type Electrodes. *Journal of Nanoscience and Nanotechnology* 12 (5): 4163–67.
- Hossain, N., S. Das, T. L. Alford (2016). An Approach to Equivalent Circuit Modelling of Inverted Organic Solar Cells. *Circuits and Systems* 07 (08): 1297–1306.
- Jeong, J.A., H. K. Kim, D. Y. Kim, S. Na, Y. S. Park, K. H. Choi and H. K. Park. (2009). Comparative Investigation of Transparent ITO/Ag/ITO and ITO/Cu/ITO Electrodes Grown by Dual-Target DC Sputtering for Organic Photovoltaics. *Journal of The Electrochemical Society*. 156 (7): H588.
- Kerkache, L., A. Layadi, E. Dogheche and D. Rémiens. (2006). Physical Properties of RF Sputtered ITO Thin Films and Annealing Effect. *Journal of Physics D: Applied Physics* 39 (1): 184–89.
- Kim, E. H., C. W. Yang and J. W. Park. (2011). The Crystallinity and Mechanical Properties of Indium Tin Oxide Coatings on Polymer Substrates. *Journal of Applied Physics*. 109 (4): 043511-043511–18.

- Kim, Soo Young, Jong-Lam Lee, Ki-Beom Kim, and Yoon-Heung Tak. 2004. "Effect of Ultraviolet–Ozone Treatment of Indium–Tin–Oxide on Electrical Properties of Organic Light Emitting Diodes." *Journal of Applied Physics* 95 (5): 2560–63.
- Klein, Andreas. (2000). Electronic Properties of In₂O₃ Surfaces. *Applied Physics Letters* 77 (13): 2009–11.
- Koseoglu, H., F. Turkoglu, M. Kurt, M. D. Yaman, F. G. Akca, G. Aygun, and L. Ozyuzer. (2015). Improvement of Optical and Electrical Properties of ITO Thin Films by Electro-Annealing. *Vacuum*. 120: 8–13.
- Kurz, A. and M.A. Aegerter. (2008). Novel Transparent Conducting Sol-Gel Oxide Coatings. *Thin Solid Films*. 516 (14): 4513–18.
- Langley, D., G. Giusti, C. Mayousse, C. Celle, D. Bellet and J. P. Simonato. (2013). Flexible Transparent Conductive Materials Based on Silver Nanowire Networks: A Review. *Nanotechnology*. 24 (45): 452001.
- Lee, J. Y., J. W. Yang, J. H. Chae, J. H. Park, J. I. Choi, H. J. Park, and D. Kim. (2009). Dependence of Intermediated Noble Metals on the Optical and Electrical Properties of ITO/Metal/ITO Multilayers. *Optics Communications*. 282 (12): 2362–66.
- Lee, J. H., K. Y. Woo, K. H. Kim, H. D. Kim and T. G. Kim. (2013). ITO/Ag/ITO Multilayer-Based Transparent Conductive Electrodes for Ultraviolet Light-Emitting Diodes. *Optics Letters*. 38 (23): 5055.
- Løvvik, O. M., S. Diplas, A. Romanyuk and A. Ulyashin. 2014. Initial Stages of ITO/Si Interface Formation: In Situ x-Ray Photoelectron Spectroscopy Measurements upon Magnetron Sputtering and Atomistic Modelling Using Density Functional Theory. *Journal of Applied Physics* 115 (8): 083705.
- Swann, S. (1988). Magnetron Sputtering. *Physics in Technology*. 19:67
- Mason, T. O., G. B. Gonzalez, D. R. Kammler, N. Mansourian-Hadavi, and B. J. Ingram. (2002). Defect Chemistry and Physical Properties of Transparent Conducting Oxides in the CdO-In₂O₃-SnO₂ System. *Thin Solid Films* 411 (1): 106–14.

- Mizubayashi, H. and S. Okuda. (1989). Structural Relaxation Induced by Passing Electric Current in Amorphous Cu₅₀Ti₅₀ at Low Temperatures. *Physical Review*. B 40 (11): 8057–60.
- Monshi, A., M. R. Foroughi, M. R. Monshi. (2012). Modified Scherrer Equation to Estimate More Accurately Nano-Crystallite Size Using XRD. *World Journal of Nano Science and Engineering*. 02 (03): 154–60.
- Ou, S. L., D. S. Wu, S. P. Liu, Y. C. Fu, S. C. Huang and R. H. Horng. (2011). Pulsed Laser Deposition of ITO/AZO Transparent Contact Layers for GaN LED Applications. *Optics Express* 19 (17): 16244.
- Pei, Y., L. Lin, W. Zheng, Y. Qu, Z. Huang, and F. Lai. (2009). Effect Of Passing Electric Current On The Electrical And Optical Properties Of ITO Films in Air. *Surface Review and Letters*. 16 (06): 887–93.
- Rakhshani, A. E., Y. Makdisi and H. A. Ramazaniyan. (1998). Electronic and Optical Properties of Fluorine-Doped Tin Oxide Films. *Journal of Applied Physics* 83 (2): 1049–57.
- Rogozin, A., N. Shevchenko, M. Vinnichenko, M. Seidel, A. Kolitsch and W. Möller. (2006). Annealing of Indium Tin Oxide Films by Electric Current: Properties and Structure Evolution. *Applied Physics Letters* 89 (6): 061908.
- Sca, J. H., H. C. Theuerer, H. C. Torrey, C. A. Whitmer, W. H. Brattain, J. Bardeen, (1948). Letters To The Editor For Methods of Preparation and Information on the Rectifier, See Nature of the Forward Current in Germanium Point Contacts.
- Shanthi, E., A. Banerjee, V. Dutta, and K. L. Chopra. (1982). Electrical and Optical Properties of Tin Oxide Films Doped with F and (Sb+F). *Journal of Applied Physics*. 53 (3): 1615–21.
- Shockley, W., (1949). The Theory of p-n Junctions in Semiconductors and p-n Junction Transistors. *Bell System Technical Journal* 28 (3): 435–89.
- Sibin, K P, N. Selvakumar, A. Kumar, A. Dey, N. Sridhara, H. D. Shashikala, A. K. Sharma, and H. C. Barshilia. (2017). Design and Development of ITO/Ag/ITO Spectral Beam Splitter Coating for Photovoltaic Thermoelectric Hybrid Systems. *Solar Energy* 141: 118–26.

- Singh, V., D. Joung, L. Zhai, S. Das, S. I. Khondaker and S. Seal. (2011). Graphene Based Materials: Past, Present and Future. *Progress in Materials Science* 56 (8): 1178–1271.
- Song, P. K., H. Akao, M. Kamei, Y. Shigesato and I. Yasui. (1999). Preparation and Crystallization of Tin-Doped and Undoped Amorphous Indium Oxide Films Deposited by Sputtering. *Japanese Journal of Applied Physics* 38 (Part 1, No. 9A): 5224–26.
- Srivastava, Manish. n.d. “Physics of Semiconductor Devices.” Accessed June 15, 2019. https://www.academia.edu/9399823/Physics_of_Semiconductor_Devices.
- Stankovich, S., D. A. Dikin, G. H. B. Dommett, K. M. Kohlhaas, E. J. Zimney, E. A. Stach, R. D. Piner, S. T. Nguyen and R. S. Ruoff. (2006). Graphene-Based Composite Materials. *Nature*. 442 (7100): 282–86.
- Terasako, T., M. Yagi, M. Ishizaki, Y. Senda, H. Matsuura and S. Shirakata. (2007). Growth of Zinc Oxide Films and Nanowires by Atmospheric Pressure Chemical Vapor Deposition Using Zinc Powder and Water as Source Materials. *Surface and Coatings Technology*. 201 (22-23): 8924-30.
- Tuna, O., Y. Selamet, G. Aygun and Lutfi Ozyuzer. (2010). High Quality ITO Thin Films Grown by Dc and RF Sputtering without Oxygen. *Journal of Physics D: Applied Physics* 43 (5): 055402.
- Turkoglu, F., H. Koseoglu, S. Zeybek, M. Ozdemir, G. Aygun, and L. Ozyuzer. (2018). Effect of Substrate Rotation Speed and Off-Center Deposition on the Structural, Optical, and Electrical Properties of AZO Thin Films Fabricated by DC Magnetron Sputtering. *Journal of Applied Physics*. 123 (16).
- “X-Ray Diffraction (XRD): Anton Paar Wiki.” Accessed June 20, 2019. <https://wiki.anton-paar.com/en/x-ray-diffraction-xrd>